THE JOURNAL OF PHYSICAL CHEMISTRY C
Cite This: J. Phys. Chem. C XXXX, XXX, XXX−XXX
Feature Article
pubs.acs.org/JPCC

Traversing Energy Landscapes Away from Equilibrium: Strategies for Accessing and Utilizing Metastable Phase Space

Abhishek Parija,[†,‡,§] Gregory R. Waetzig,[†] Justin L. Andrews,[†] and Sarbajit Banerjee*,[†]

[†]Department of Chemistry and Department of Materials Science and Engineering, Texas A&M University, College Station, Texas 77845-3012, United States

[‡]Molecular Foundry, Lawrence Berkeley National Laboratory, Berkeley, California 94720, United States

[§]Advanced Light Source, Lawrence Berkeley National Laboratory, Berkeley, California 94720, United States

Web-Enhanced Feature

ABSTRACT: The known crystal structures of solids often correspond to the most thermodynamically stable arrangement of atoms. Yet, oftentimes there exist a richly diverse set of alternative structural arrangements that lie at only slightly higher energies and can be stabilized under specific constraints (temperature, pressure, alloying, point defects). Such metastable phase space holds tremendous opportunities for nonequilibrium structural motifs and distinctive chemical bonding and ultimately for the realization of novel function. In this Feature Article, we explore the challenges with the prediction, stabilization, and utilization of metastable polymorphs. We review synthetic strategies that allow for trapping of such states of matter under ambient temperature and pressure including topochemical modification of more complex crystal structures; dimensional confinement wherein surface energy differentials can alter bulk phase stabilities; templated growth exploiting structural homologies with molecular precursors; incorporation of dopants; and application of pressure/strain followed by quenching to ambient conditions. These synthetic strategies serve to selectively deposit materials within local minima of the free-energy landscape and prevent annealing to the thermodynamic equilibrium. Using two canonical early transition-metal oxides, HfO_2 and V_2O_5, as illustrative examples where emerging synthetic strategies have unveiled novel polymorphs, we highlight the tunability of electronic structure, the potential richness of energy landscapes, and the implications for functional properties. For instance, the tetragonal phase of HfO_2 is predicted to exhibit an excellent combination of a high dielectric constant and large band gap, whereas ζ-V_2O_5 has recently been shown to be an excellent intercalation host for Mg batteries. Despite recent advances, the discipline of metastable periodic solids still remains substantially dependent on empiricisms given current inadequacies in structure prediction and limited knowledge of energy landscapes. The close integration of theory and experiment is imperative to transcend longstanding chemical bottlenecks in the prediction, rationalization, and realization of new chemical compounds outside of global thermodynamic minima.

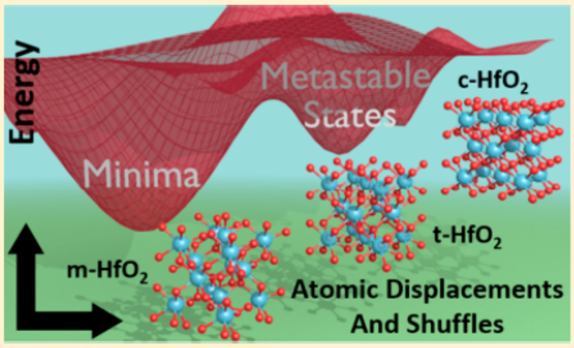

1. INTRODUCTION

The design of new compounds with properties tailored to exhibit specific function is a grand challenge in the physical sciences but is greatly hindered by the immense span of the terra incognita, spanning ternary, quaternary, and more complex combinations across the periodic table that remain almost entirely unexplored. Limiting the search for specific function to current crystallographic databases essentially corresponds to sampling of a sparse and often fairly random set of possibilities across multidimensional configurational landscapes and not surprisingly has been of limited utility. One alternative involves examining hypothetical compounds; however, predicting the structure of a crystalline compound given just its composition continues to be a formidable challenge that has considerably limited the scope of computationally aided materials design.[1−3] Increasingly efficient treatments of electron densities and energies in density functional theory (DFT) have enabled the accurate prediction of a variety of structure-dependent properties for periodic solids; however, when the structure of a compound under a given set of conditions is not known, the a priori prediction of its properties becomes rather difficult. Approaches for crystal structural prediction from first-principles tend to emphasize searching for the minimum energy structural arrangement of atoms, which while useful, neglect the considerable range of new functionality potentially accessible within metastable polymorphs, the identification of energetically proximate bistable wells whose reversible transformations can allow for switching of properties, and the recognition of specific structural motifs that could underpin specific functionality. From a fundamental perspective, the search for lowest energy structures often

Received: May 15, 2018
Revised: June 27, 2018
Published: July 6, 2018

DOI: 10.1021/acs.jpcc.8b04622
J. Phys. Chem. C XXXX, XXX, XXX−XXX

constrains ideas of chemical bonding to equilibrium forms.[4−6] Indeed, constructs such as formal oxidation states, coordination preferences, and the extent of covalency/ionicity constitute the fundamental tenets of chemistry and are often used to rationalize structure and reactivity. However, much of the conventional chemical intuition on these matters tends to be derived from the behavior of compounds at equilibrium. Metastable compounds in close proximity to thermodynamic equilibria can manifest starkly different behavior from their equilibrium counterparts and thereby provide access to a diversity of atomic arrangements and chemical bonding and function much richer than accessible when considering equilibrium configurations alone.[4,7−10] Such structures are often characterized by electronic structure peculiarities, closely coupled electron and lattice degrees of freedom, and magnetic frustration, which are a direct result of the stabilization of unusual oxidation states, multicenter bonding, and topologically enforced coordination environments; these characteristics, in turn, underpin the manifestation of unusual physical phenomena and reactivity. In this Feature Article, we review strategies for exploring metastable phase space with an emphasis on recent progress in expanding the available repertoire of metastable phases of two canonical early transition-metal oxides, HfO_2 and V_2O_5. The two represent an interesting study in contrast; the former is characterized by relatively deep wells positioned relatively far apart on the energy landscape (a "smooth" landscape with only a few polymorphs as illustrated in Figure 1), whereas the latter is characterized by numerous closely positioned polymorphs (conceptualized as a "rugged" energy landscape with scores of shallow wells). Placing the two illustrative systems in the broader perspective of synthetic strategies deployed to access metastable compounds, we discuss the opportunities that become available when composition does not result in structural destiny.

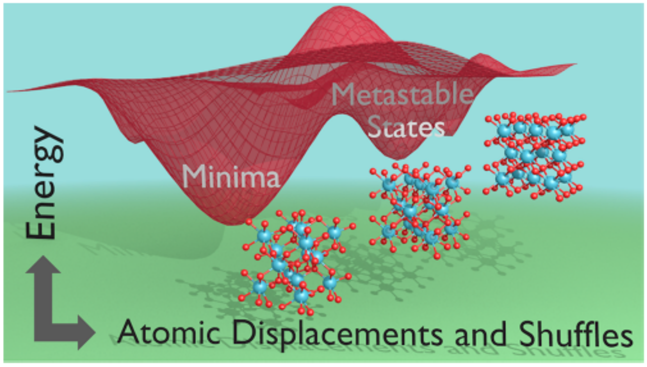

Figure 1. Schematic illustration of a "smooth" energy landscape with distinctly separated wells corresponding to the thermodynamically stable phase and two metastable polymorphs. Several polymorphs of HfO_2 are depicted in the sketch; the monoclinic phase represents the thermodynamic minimum, whereas tetragonal and cubic polymorphs are accessible at temperatures of ca. 1700 and ca. 2200 °C, respectively.

Metastable compounds that represent local minima on the energy landscape have specific features that render them higher in energy as compared with the global minimum (Figure 1). Such features span the gamut from unfavorable "frustrated" coordination geometries to strained bonding of structural units (e.g., arising from the rigidity of polyanionic units) and elements of electron correlation and magnetic frustration. Despite such intrinsic instabilities, their position on the energy landscapes often renders them isolable and even "bottle-able" when (a) the path and angle of descent in the multidimensional energy landscape are controlled during synthesis to deposit the material in a shallow metastable well from which it cannot readily be dislodged or (b) upon perturbation of thermodynamically stable structures along specific coordinates such as through the application of pressure, or alternately, chemical pressure/strain induced by incorporating dopants.

Metastable phases characterized by unusual bonding motifs can often be deployed to realize new functionality. Diamond presents an iconic example of a metastable phase and is a high-pressure metastable allotrope of carbon that can nonetheless be kinetically trapped and stabilized under ambient temperature and pressure conditions; its covalent sp^3-bonded network yields remarkable hardness that finds a wide variety of industrial applications for drilling and cutting of other materials.[11,12] In a similar vein, whereas the 2H phase of MoS_2 is the thermodynamically stable phase in the bulk, a metallic 1T phase is stabilized as a result of the decreased formal oxidation state of molybdenum centers upon Li-ion intercalation and shows vastly improved activity as an electrocatalyst for the hydrogen evolution reaction.[13−15] A trigonal prismatic $[MoS_6]$ coordination geometry is preferentially adopted when the Mo center has a $3d^2$ electronic configuration, whereas the octahedral $[MoS_6]$ coordination geometry is stabilized with a $3d^3$ configuration. The remarkable performance of olivine Li_xFePO_4 as a cathode material at high rates was initially puzzling given the poor miscibility of Li-rich and Li-poor Li_xFePO_4 phases until the discovery that for small particle sizes the energy dissipative nucleation and growth of the Li-rich phase is circumvented by instead stabilizing a metastable solid-solution phase that continuously incorporates lithium ions; solid-solution formation circumventing phase segregation has indeed been predicted to be fairly generalizable to a variety of cathode materials below a critical size.[16,17] The stabilization of metastable austenitic phases is furthermore well known in ferrous metallurgy, wherein phase transformations to thermodynamically stable phases provide a means of energy dissipation and toughening upon the application of mechanical strain.[18,19]

Metastable compounds have thus far typically been discovered through a combination of serendipity and ad hoc exploratory synthesis.[20,21] Hence, crucially missing is the fundamental understanding of which metastable materials can be successfully synthesized, design rules for stabilizing such polymorphs, mapping of transformation pathways between polymorphs (toward or further away from equilibrium), and an understanding of how their specific structural motifs and potential transformations can be harnessed to realize novel function.[22−24] We start by reviewing some fundamental governing physical principles and highlighting some illustrative examples. Next, through the specific case studies of V_2O_5 and HfO_2, we demonstrate synthetic strategies, tunability of electronic structure, and functional implications of stabilizing such compounds.

2. PREDICTING VIABLE METASTABLE COMPOUNDS AND THEIR TRANSFORMATIONS

2.1. Structure Prediction and Identification of Viable Polymorphs. In light of the vast configurational possibilities for stabilizing different structural arrangements given a specific composition, it is important to develop design rules for predicting structure and exploring energy landscapes to a priori identify viable metastable frameworks for stabilization. Such an approach is imperative to facilitate initial screening for functionality using first-principles calculations as well as to guide synthetic prioritization. As a notable example of evolutionary

DOI: 10.1021/acs.jpcc.8b04622
J. Phys. Chem. C XXXX, XXX, XXX−XXX

algorithm approaches, Zurek and coworkers have developed XtalOpt,[25] which coupled to DFT calculations has been used to successfully predict a variety of metastable phases stabilized under constraints such as high pressure. For instance, this approach has recently been used to predict the structure of PH_2 phases found to be superconducting at high pressures[26] as well as to predict the existence and manifestation of superconductivity within a metastable $I4/mmm$-$BaGe_3$ phase.[27] The superconductivity of the latter phase has indeed now been experimentally verified, which represents a major milestone for first-principles structure prediction.[28] In another approach,[29] Stevanović performed DFT calculations on a large set of random superlattices of MgO, ZnO, and SnO_2 crystal systems to successfully predict the probability of the occurrence of a given structure, which, in turn, is reflective of the accessible metastable polymorphs in these systems. The development of materials property databases powered by high-throughput first-principles calculations has provided additional opportunities for the use of machine learning to extract correlative patterns across large data sets.[30−33] One notable insight from these studies suggests that the most viable metastable polymorphs are those that represent the energetically lowest polymorphs under a specific set of constraints (e.g., temperature, chemical potential, surface confinement, tensile or compressive stress); rapid quenching of these structures upon the removal of the constraint can leave the metastable phases trapped within shallow valleys.[34,35] From a practical perspective, if constraints under which a considered phase is the energetic minimum cannot be identified, then devising a synthetic strategy becomes rather challenging.

2.2. Explorations of Transformation Pathways. The pathways along which metastable polymorphs traverse to the thermodynamic minimum or to other polymorphs determine the energetic barriers and thus their accessibility and stability. Energetically proximate polymorphs are of particular interest as a result of their being switchable upon the application and removal of external stimuli. For instance, the metal—insulator transitions of VO_2 and NbO_2 are accompanied by monoclinic to tetragonal and undistorted rutile to body-centered distorted rutile transitions, respectively.[6,36,37] Energetic proximity is, of course, a necessary but not sufficient criterion for obtaining bistable systems; the energy barriers for transitions between two phases are fundamentally a function of the pathway linking the two polymorphs. The barriers between the insulating and metallic phases in these materials, reflective of varying structural and electronic contributions, are vastly different, as reflected in transition temperatures of 67 and 807 °C in VO_2 and NbO_2, respectively. The determination of energy landscapes and transformation paths is thus critical to accessing metastable polymorphs. While exceedingly computationally expensive given the multiple degrees of freedom, calculations of energy landscapes as a function of structural degrees of freedom, taking into account potential constraints such as templates, strain, finite size, or surface confinement, can provide important inputs to synthetic strategies.

The generalized solid-state nudged elastic band formalism is one of the most commonly used algorithms to successfully predict minimal energy transformations; it allows for the computation of the structure and energetics of transition states and thereby allows for evaluation of the energetic barriers and kinetics of polymorphic transformations.[38−40] However, a primary drawback of NEB-based approaches is the requirement of an a priori assumption with regards to the initial and final states of the transformation. Recently, Stevanović and coworkers[24] have developed a structure mapping algorithm, which uses an optimal mapping approach that is diffusionless in nature and minimizes the dissociation of chemical bonds. In another example, Arroyave and coworkers have developed a mathematical framework for the rapid exploration of energy landscapes in phase-transforming materials, allowing for the identification of metastable intermediates based on the implementation of novel multidimensional string methods to identify transformation paths between arbitrary minima in the energy landscape.[41] It is anticipated that the development of more efficient algorithms and a greater deployment of high-performance computing resources will substantially increase the understanding of complete energy landscapes and allow for insights into how transformation pathways can be altered. The role of defects, strain, and dopants on transformation pathways remain underexplored, primarily owing to the computational expense of calculating landscapes for large supercells across multiple configurational degrees of freedom.

3. STRATEGIES FOR THE SYNTHESIS OF METASTABLE COMPOUNDS

3.1. Solution Phase Synthesis and Topochemical Methods. Potential energy landscapes such as plotted in Figure 1 are essentially representations of the free energy of a system plotted as a function of configurational degrees of freedom. As a system relaxes toward equilibrium, from a high-energy state, it explores the landscape in search of a means to most efficiently dissipate the excess free energy. Conventional ceramic and metallurgical processing routes provide an excess of energy, and thus the material is usually able to efficiently explore the path toward equilibrium without being trapped in metastable states. In contrast, solution-phase synthesis routes have the potential to carefully "deposit" the material in a local minimum that can effectively "trap" the system within forms exhibiting unusual chemical bonding motifs. Such local "traps" can further be modulated through the inclusion of defects, impurities, disorder, and interfaces, all of which serve to direct the trajectory of a material down its descent from a higher energy state.

Topochemical modification routes represent a particularly intriguing approach wherein leaching of specific anionic or cationic structural components provides a means of stabilizing open framework structures, which, in turn, can again be intercalated with other cations or anions such that the final structure represents the atomistic arrangements defined by the initial template.[45,46] Performing these reactions at low temperatures and with reactivities of leaching agents matched to ensure that slow diffusion assures preservation of the metastable frameworks by limiting the amount of energy available to facilitate recrystallization to the thermodynamic form. As a recent elegant example of this approach, Powell and coworkers[42] have shown that upon starting with roxbyite-type $Cu_{2-x}S$ solution-mediated cation exchange yields metastable wurtzite polymorphs of CoS and MnS (Figure 2A). As another example, the topochemical deintercalation of Ca-ions from $CaGe_2$ has allowed for stabilization of germanane, a 2D analogue of graphene.[47] Indeed, Goldberger and colleagues have recently elaborated this strategy to stabilize 1T, 2H, and 6R germanane polytypes by topochemical deintercalation of cations from 1T $EuGe_2$, 2H α-$CaGe_2$, and 6R β-$CaGe_2$ Zintl phases.[48] The reaction of GdOCl nanocrystals with XeF_2 has allowed for stabilization of a metastable GdF_3 polymorph, providing an example of topochemical alteration of the anion sublattice.[49] In a subsequent section, we discuss at some length the myriad V_2O_5 polymorphs that can be accessed using topochemical methods.

DOI: 10.1021/acs.jpcc.8b04622
J. Phys. Chem. C XXXX, XXX, XXX−XXX

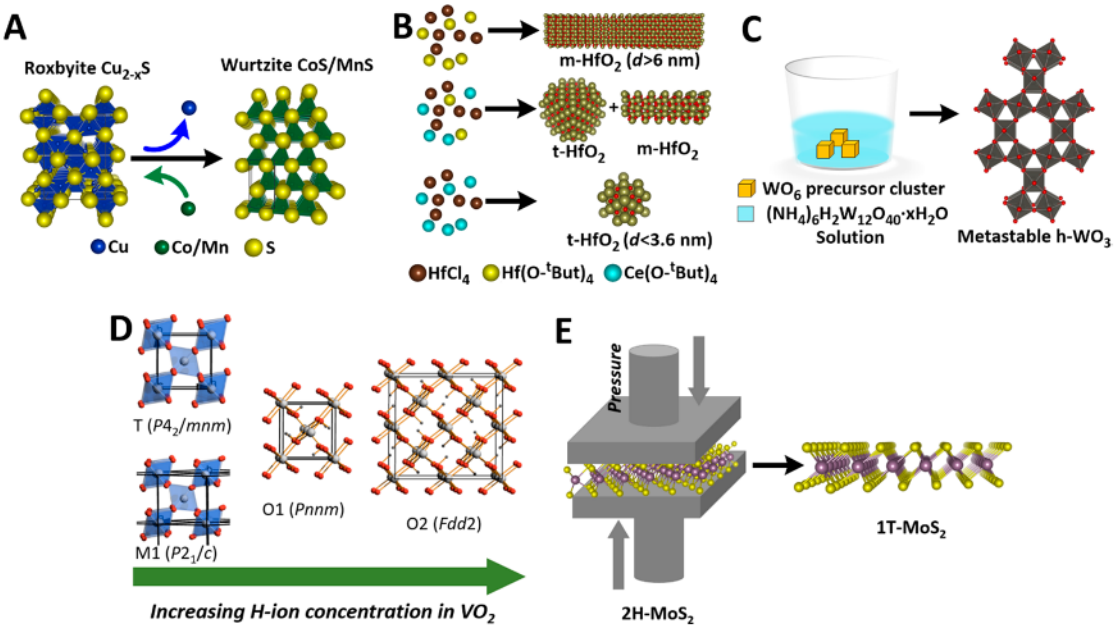

Figure 2. Schematic illustration of strategies for the stabilization of metastable polymorphs: (A) Topochemical modification: Roxbyite-$Cu_{2-x}S$ is topochemically converted to the metastable wurtzite polymorphs of CoS and MnS via solution-mediated cation exchange.[42] (B) Dimensional confinement: The metastable tetragonal phase is stabilized below a critical size of ca. 3.6 nm. (C) Templated growth: The metastable hexagonal WO_3 phase is stabilized by templated growth of WO_6 nuclei in a precursor solution of $(NH_4)_6H_2W_{12}O_{40}{\cdot}xH_2O$.[43] (D) Dopant incorporation: increasing interstitial doping of hydrogen in M1 ($P2_1/c$) phase of VO_2 stabilizes the metastable O1 ($Pnnm$) and O2 ($Fdd2$) phases, respectively. Adapted with permission from ref 67. Copyright 2014 American Chemical Society. (E) Pressure: A pressure-induced structural distortion accompanied by a semiconducting—metallic electronic transition is achieved during the conversion of 2H-MoS_2 to 1T-MoS_2.[44]

3.2. Finite Size Effects on Phase Stability.

Surfaces and dimensional confinement provide the second primary strategy for the synthesis of metastable polymorphs. At nanoscale dimensions, surface free-energy (as well as strain energy) terms can be opposite in sign to bulk free-energy descriptors and enable the stabilization of unusual structural motifs under conditions that represent constrained equilibrium rather than kinetic trapping.[4,8] The size dependence of free energy can be written as

$$G^{\circ} = G_{\text{bulk}} + \sum_i \gamma_i A_i \tag{1}$$

where G_{bulk} is the bulk free energy and γ and A are the surface energy and surface area of a given facet i.[4] If there are two polymorphs a and b, for which $G_a < G_b$ but $\gamma_b < \gamma_a$, then the differences in surface energy can bring about a crossover of thermodynamic phase stabilities below a certain critical size. For example, the rutile phase of TiO_2, with $P4_2/mnm$ symmetry, become more stable than the anatase phase, with $I4_1/amd$ symmetry, at a critical diameter of ca. 14 nm.[50] More than 50 years ago, Garvie discovered that below a grain size of 30 nm ZrO_2 can be stabilized in the tetragonal phase at room temperature. This remarkable stabilization originates from the surface energy contribution outweighing the bulk free energy because the tetragonal phase exposes considerably lower energy surface facets.[51,52] A full account of the different energy terms involved in the phase transformation is warranted to understand the pronounced size dependence of phase stability; the relevant terms will be contrasted in a subsequent section to highlight the differences between HfO_2 and ZrO_2, which has made stabilization of high-temperature polymorphs of the former a much more challenging endeavor.[53,54] In contrast with ZrO_2, the critical size for stabilization of tetragonal HfO_2 is found to be almost an order of magnitude lower, ca. 3.6 nm, as shown in Figure 2B.

3.3. Templated Growth.

A third approach involves nucleation and growth of materials from specific epitaxially matched templates that favor the growth of a metastable polymorph over the thermodynamically stable phase. The growth of metastable phases under these conditions reflects the strain-induced crossover of thermodynamic stability in specific systems and is an interesting corollary to pressure-induced transitions. Classical examples include stabilization of α-Sn and α-Sn:Ge alloys using molecular beam epitaxy.[55] Similarly, MgS and MnS have been grown in the metastable zinc-blende phase by molecular beam epitaxy onto GaAs (100) substrates.[56] An insulating metastable monoclinic M2 phase is stabilized under strain for VO_2 thin films and individual nanorods;[57] indeed, a solid-state "triple point" has been identified wherein the M2 phase as well as the insulating monoclinic M1 phase (the thermodynamic minimum) and a rutile phase can coexist along a strain—temperature phase diagram.[58] Remarkably, similar strain effects have been observed upon the incorporation of W dopants within otherwise freestanding nanorods reflective in large measure of the equivalence of chemical strain; slivers of M2 domains spanning only a few unit cells are stabilized at the interface between M1 and rutile phases and minimize the strain mismatch between these polymorphs.[59,60]

As a variation on this theme, Iversen has followed the stabilization of various polymorphs of WO_3 (Figure 2C), utilizing in situ pair distribution function methods, and has demonstrated the remarkable preservation of structural motifs from molecular precursors to extended solids, reflecting a close structural relationship between the precursors and incipient nuclei that strongly alters the relative phase stabilities from the bulk phase diagram.[43] Such an idea of seeded growth wherein the final polymorph shows structural homologies to the precursor has further been noted for MnO_2 nanocrystals grown under hydrothermal conditions.[61]

3.4. Dopant Effects on Phase Diagrams. The inclusion of extrinsic dopants or variation of the concentration of intrinsic point defects can profoundly alter phase diagrams. The stabilization of cubic and tetragonal ZrO_2 by aliovalent doping is well established and is a result of the altered local coordination environments,[62] oxidation states, and size of the dopant atoms that are oftentimes better accommodated in a higher energy metastable polymorph as compared with the (often close-packed) phase that represents the thermodynamic minimum. Ramprasad has recently presented a detailed computational exploration of dopants that can potentially stabilize the ferroelectric orthorhombic phases of HfO_2.[63,64] Such studies are illustrative of approaches for the rational design of doping schemes that are thus far only sparsely explored.

An intriguing set of ideas that has attracted recent attention is the use of diffusive dopants to reversibly alter phase stabilities, providing a means to access metastable phase space through postsynthetic modification. By coupling the diffusion of dopants to applied strain, chemical potential gradients, or voltage fields, the phase of a material can be changed "on the fly", thereby providing a powerful means of dynamically modifying phase diagrams. In recent work, voltage-driven insulator (2H)—metal (1T′) transitions have been evinced in $MoTe_2$ upon electrostatic modulation; electrostatic doping can be induced through intercalation of Li-ions instead of direct electrical biasing of the 2D materials.[65,66] Other examples of diffusive dopants that alter phase stability are observed for hydrogen (Figure 2D) and boron interstitial dopants in VO_2; the former stabilizes an orthorhombic phase, whereas the latter stabilizes the rutile metallic phase.[67,68]

3.5. Pressure-Induced Stabilization of Metastable Phases. The pressure applied on materials can be tuned suitably to unravel novel metastable phase space. Indeed, Nayak and coworkers, have demonstrated the conversion of the thermodynamically stable 2H-phase of MoS_2 to the 1T-phase upon the application of pressure.[44] A structural distortion, followed by an electronic transition from semiconducting to metallic state, has been observed at ca. 19 GPa (Figure 2E). Ab initio calculations reveal an increased overlap of the valence and conduction bands due to compression as the possible origin of the phase transition. In another example, Flores-Livas and researchers have been able to synthesize multiple metastable phases of phosphorus by applying pressure up to 170 GPa.[69] Several of the metastable phases showed excellent superconducting properties, entirely inaccessible in the thermodynamically stable-phase red phosporous. Applying high pressure in conjunction with moderate temperature can easily overcome the barrier to stabilize metastable polymorphs. For example, the high-pressure phase β-V_2O_5 can be synthesized by coupling temperature and pressure.[70]

4. ELUCIDATING STRUCTURE—FUNCTION CORRELATIONS ACROSS POLYMORPHS

When comparing a metastable material to its thermodynamically stable counterpart, it is important to note that the stoichiometry, constituent elements, and generally the formal valence states of the elements that comprise the material remain the same; only the specific ordering and connectivity of the material changes, and thus utilizing metastable polymorphs represents a means to directly alter the arrangement of the atoms of a material in physical space. The altered connectivity can have a pronounced influence on the local bonding, strongly altering the ionicity/covalency of the framework[71] and giving rise to a vastly different electronic structure. Such structures can thus allow for substantial tunability of electronic, magnetic, and optical properties.

A detailed elucidation of chemical bonding across different polymorphs can further delineate structural (and bonding) motifs from the equilibrium structure that are conserved in accessible metastable frameworks, and, conversely, those "free-energy raising" features that represent excursions from the thermodynamic minima that are still accessible. The identification of structural motifs that underpin a certain function furthermore provides design rules for targeted exploration of phase space. As we will discuss below, rigid connectivity of vanadium-centered polyhedra and relatively uniform coordination environments of interstitial sites facilitates diffusion of multivalent cations;[72,73] as another example, linear chains of vanadium-centered polyhedra facilitate the stabilization of metallic compounds, whereas dimerization of such chains opens a Mott—Hubbard gap.[5]

The specific role of metastability in altering structure—function relationships is perhaps nowhere more apparent than in metastable vanadium oxide materials; the accessibility of different oxidation states of vanadium and the close stabilities of tetrahedral, square pyramidal, and octahedral environments allows for the stabilization of a variety of structural motifs. In our recent work, we have explored the structure—function relationship between ionic diffusion barriers and crystallographic structure for several polymorphs of V_2O_5 with distinct structural motifs.[74,75] A detailed discussion of different V_2O_5 polymorphs is presented in the next section.

In another example, HfO_2 is known to have a combination of a high dielectric constant and large band gap,[76] making it an excellent dielectric for use within field-effect transistors. However, the thermodynamically stable monoclinic phase of HfO_2 has a dielectric constant of ∼18. In contrast, the metastable tetragonal phase of HfO_2 (stable above ca. 1700 °C) has a predicted dielectric constant of 70 and a band gap of 6 eV.[77] The change in local symmetry and coordination strongly modifies the phonon dispersion of tetragonal HfO_2 as compared with monoclinic HfO_2; the softer phonon modes of the metastable polymorphs underpin the much higher dielectric response.[78] The stabilization of metastable phases of HfO_2 is discussed in a subsequent section.

5. METASTABILITY AND INTERCALATION CHEMISTRY

5.1. Nonequilibrium Intercalation and Metastability in $LiFePO_4$ and MnO_2. Metastability—as a concept, recurring motif, and design tool—[73,74] is deeply intertwined in intercalation chemistry and has become increasingly important, particularly with the rise of secondary batteries exploiting intercalation phenomena. Indeed, the success of the Li-ion battery is founded on the use of materials that in their fully charged states are in fact metastable[79] or alternatively pass through metastable intermediate states, thereby circumventing immiscibility gaps and eschewing energetically costly nucleation and growth mechanisms.[16,80] More specifically, in the case of lithium cobalt oxide and related cathode materials, full cells are typically assembled using the thermodynamically stable discharged phases ($LiCoO_2$). Upon charging, metastable materials of the type $Li_{1-x}CoO_2$ are formed as x approaches unity, albeit the depth of discharge is typically limited to $x = 0.5$ to avoid oxygen evolution due to surface peroxide formation.[79,81,82] In the case of Li_xFePO_4, both end members (i.e., $FePO_4$ and $LiFePO_4$) are thermodynamically stable; however, there is severely limited Li solubility in both phases, which suggests that lithiation/deliathiation proceeds according to nucleation and growth of the fully lithiated phase growing at the expense of the delithiated phase.[83] Below a certain particle size regime, however, much higher rates are observed. The increased rates in smaller particles have been attributed to the stabilization of metastable compositions (with increased Li solubility) that bridge the miscibility gap of the thermodynamically stable end members to allow for complete solid-solution formation across the entire cycling range (i.e., $0 < x < 1$ in Li_xFePO_4).[80,84]

Perhaps more recognized is the utilization of various polymorphs of a given composition as cathode materials in attempts to vary the function while retaining composition. Indeed, this approach is ubiquitous in the exploration of novel cathode materials, particularly in the case of MnO_2, where several polymorphs such as α-MnO_2 and δ-MnO_2 are directly accessible from hydrothermal synthesis.[61,85] In other cases, metastable binary materials are stabilized via selective removal of an ionic species (e.g., stabilization of metastable λ-MnO_2 by extraction of Li from the thermodynamically stable $LiMn_2O_4$ spinel-type structure).[86,87] Indeed, such an approach provides access to a broad palette of Mn−O connectivity encompassing polymorphs with 3D (β-MnO_2, thermodynamic minimum), 2D (δ-MnO_2, spinel λ-MnO_2), and quasi-1D (hollandite α-MnO_2, ramsdellite R-MnO_2, and γ-MnO_2) crystal structures.[88] Despite the extensive use of these materials as cathode materials, no generalized approach to their discovery has been proposed in the literature.

Finally, there has recently been increased attention to moving beyond Li toward multivalent-ion batteries (Mg^{2+}, Ca^{2+}, Zn^{2+}, Al^{3+}),[73,75,89,90] each of which has distinct inherent benefits such as the storage of twice the electrons per intercalated ion, increased safety, increased crustal abundance (and thereby decreased cost and greater sustainability), and the prospect of utilizing metal anodes (a prospect precluded in the design of Li-ion batteries as a result of safety considerations with handling metallic lithium). As we have recently shown,[73] the use of metastable materials as cathodes in multivalent ion intercalation batteries can give rise to many interesting properties derived from the fact that both the "charged" oxide (MO_x, where M is a redox-active transition metal) and the discharged phases ($M'MO_x$, where M′ is an electrochemically intercalated multivalent cation) are metastable. Indeed, in the case of the recently studied β-$Mg_{0.33}V_2O_5$−ζ-V_2O_5 system, the entire compositional range is metastable. Recent success examining metastable compositions as cathode materials and the structure−function relationships that arise will be discussed below with an eye toward seeking fundamental descriptors for the design and stabilization of additional cathode materials.

5.2. Metastable Vanadium Oxides as Intercalation Hosts. Metastable phase space is vast when compared with thermodynamically stable phase space, notionally encompassing different possible configurations of atoms, and therefore is difficult to explore in a systematic manner without computational guidance or chemical intuition.[34] One example of the latter approach, as observed in the case of spinel-derived λ-MnO_2, is to realize unique binary connectivity (i.e., MO_x where M = V, Cr, Mn, Fe, Ni, Co) from motifs observed in thermodynamically stable ternary phases (i.e., $M''MeO_x$, where M″ is a third cation—not necessarily the one that is sought to be intercalated). Such an approach is predicated on the stability of the M—O frameworks and allows for established soft-chemistry synthetic techniques to be used to remove the intercalated ions from known ternary phases to stabilize metastable binary phases. The topochemically stabilized frameworks represent kinetically trapped species that under reaction conditions are unable to recrystallize into the thermodynamically stable form; such an approach provides a considerable set of target structures for the exploration of metastability. Figure 3 illustrates a broad palette of ternary $M_xV_2O_5$ and topochemically modified V_2O_5 structures either realized experimentally or examined using first-principles calculations.

The multiple available redox states ($V^{5+} \rightarrow V^{4+} \rightarrow V^{3+}$), the high oxidizing potential of the redox couples (ca. 3.8 V vs Li), and the large theoretical specific capacity (443 mAh g^{-1} for $Li_3V_2O_5$) make V_2O_5 an exceedingly promising system from the perspective of energy-storage metrics. The large number of structural motifs and plethora of observed vanadium−oxygen connectivity and coordination observed in binary vanadium oxide materials have few parallels in other transition metals.[91] The observed structural diversity grows exponentially when moving beyond binary vanadium oxides to consider ternary vanadium oxide bronzes. The presence of intercalated cations forces the rearrangement of the vanadium oxide lattice, often resulting in unique structural motifs that are highly dependent on the identity and stoichiometry of the intercalated cation. Indeed, the intercalation of cations into V_2O_5 results in the formation of ternary $M_xV_2O_5$ (or for that matter other mixed valence $M_xV_yO_z$) materials, where the identity of "M" spans several groups of the periodic table from alkali[92−96] and alkaline metals,[97,98] to transition metals[99−101] and post-transition-metal main group cations[98] and even organic cations.[102,103] Whittingham and coworkers have exhaustively reviewed and systematically categorized the diversity of vanadium−oxygen structural connectivity, with an emphasis on open frameworks.[91] Many of these structures can potentially be fully or partially deintercalated to form metastable binary vanadium oxides with a broad range of vanadium−oxygen connectivity not observed in the thermodynamically stable layered phase of V_2O_5. These compounds suggest a powerful starting point for fundamental explorations of a "rugged" energy landscape with multiple accessible members, each with its own electronic structure and specific diffusion pathways for intercalated cations.

To date, there are six known polymorphs of V_2O_5. In addition to the thermodynamically stable α-V_2O_5 phase (Figure 3a, center),[104] there are five metastable polymorphs of V_2O_5, including the high-pressure β-V_2O_5 phase (Figure 3e), the chimie-douce-stabilized γ'-V_2O_5 (Figure 3b),[105] the close-packed-3D high-pressure δ-V_2O_5,[106] the ε'-V_2O_5 double-layered phase closely related to the xerogel phase (Figure 3d),[71] and the tunnel-structured 1D polymorph ζ-V_2O_5 (Figure 3c).[71,73,107] Although metastable, the structure of δ-V_2O_5 is close-packed, as would be expected for a polymorph stabilized above 8.5 GPa and 1100 °C.[106] A broader palette of potential metastable compounds notionally derived along the lines of Figure 3 has been examined as potential intercalation hosts using first-principles calculations.

5.3. Crystallographic Relationships and First-Principles Evaluation of Thermodynamic and Kinetic Aspects of Intercalation. Selecting ternary $M_xV_2O_5$ phases as initial precursor structures mitigates a primary issue with computational screening that often yields predicted structures that are not synthetically viable. Given the complexity involved in synthetic stabilization and electrochemical measurements, first-principles DFT calculations are nevertheless useful for evaluating the specific candidates derived from examining ternary vanadium oxides. In recent work, we have used such calculations to predict thermodynamic aspects such as structural parameters, lattice alteration upon intercalation, and open-circuit voltage as well as kinetic parameters such as diffusion

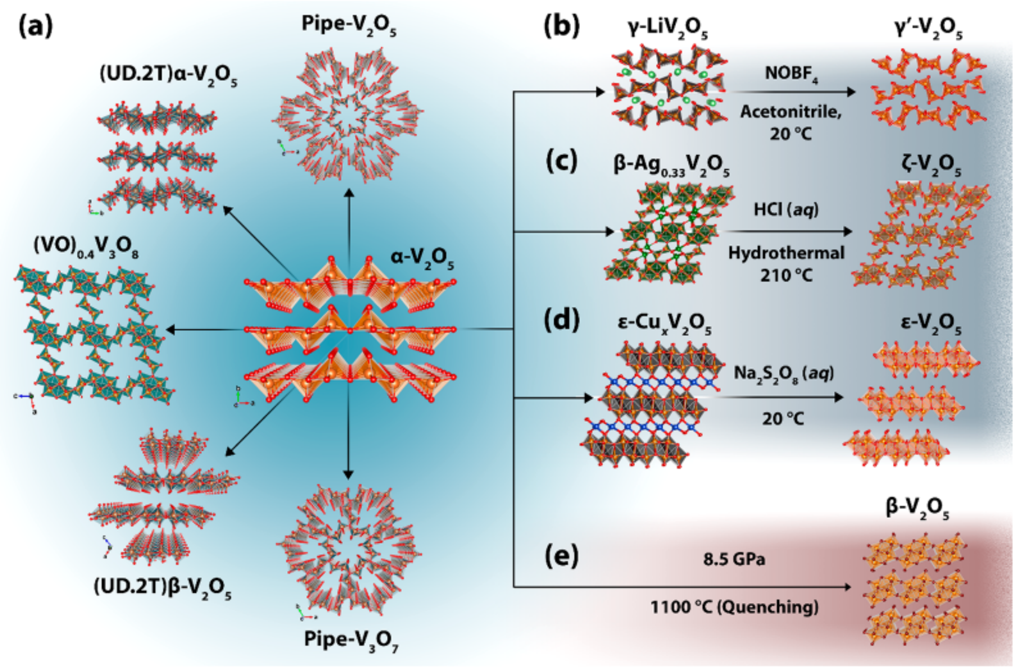

Figure 3. Metastable binary vanadium oxide phases depicted alongside parent ternary $M_xV_2O_5$ phases. (a) Thermodynamically stable α-V_2O_5 phase is depicted at the center of the schematic. Several predicted vanadium oxide phases with starkly different vanadium−oxygen connectivity are arranged on the left in a semicircle. These phases represent synthetic targets for topochemical stabilization from previously reported ternary vanadium oxide bronzes if the vanadium—oxygen connectivity of the parent compounds can be preserved upon deintercalation. Moving counterclockwise from the top of the semicircle, these ternary bronzes are $Cs_{0.3}V_2O_5$, $Ba_{0.4}(VO)_{0.4}V_2O_5{\cdot}H_2O$, CsV_2O_5, $(H_2N(C_2H_4)_2NH_2)_{0.5}V_2O_5$, and $Cs_{0.35}V_3O_7$. (b−d) Three topochemically stabilized metastable phases of V_2O_5 (γ'-, ζ-, and ε'-) delineating synthetic parameters used for topochemical deintercalation of the inserted cations from the ternary bronzes. (e) Another metastable vanadium oxide polymorph (β-V_2O_5) is depicted. This polymorph has been stabilized through application of high pressure and temperature and is stabilized at room temperature by rapid quenching (as reported in ref 70).

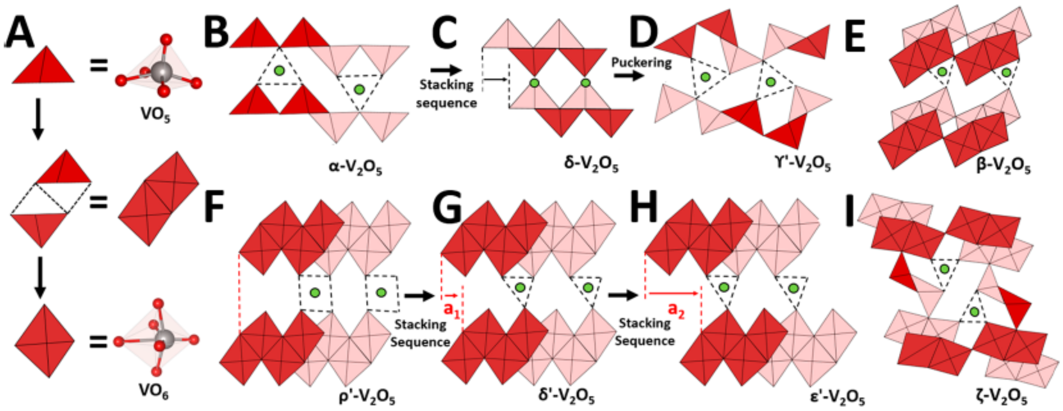

Figure 4. Schematic representation of crystallographic relationships between various polymorphs of V_2O_5. The fundamental building units of the V_2O_5 crystallographic system comprise $[VO_5]$ square pyramids and distorted $[VO_6]$ octahedral units. The gray and red spheres represent vanadium and oxygen atoms, respectively, the solid red pyramids represent $[VO_5]$ units, and the solid red quadrilaterals represent $[VO_6]$ units; a change in shading indicates that the units are in different planes. The polymorphs of V_2O_5 represented are (B) α-V_2O_5, (C) δ-V_2O_5, (D) γ'-V_2O_5, (E) β-V_2O_5, (F) ρ'-V_2O_5, (G) δ'-V_2O_5, (H) ε'-V_2O_5, and (I) ζ-V_2O_5.

barriers and diffusion pathways for various metastable polymorphs of V_2O_5.[74,75,92,108]

5.3.1. Crystallographic Relationships. α-V_2O_5 is the thermodynamic sink of the V−O phase diagram (and indeed mined as a naturally occurring ore) and is a good starting point to understand the structure of other metastable phases of V_2O_5.[109,110] It is a layered structure comprising $[VO_5]$ pyramidal units sharing corners and edges to form 2D single-layered lamellar sheets (Figure 4B). These sheets are held together by van der Waals forces along the *c* direction to form a layered crystal structure with *Pmmn* symmetry.[111] Figure 4 depicts the approximate crystallographic relationships between this structure and several metastable polymorphs. The metastable single-layered δ-V_2O_5 (thus labeled to distinguish it from the double-layered δ'-phase discussed below) with a space group symmetry of *Amma*,[104] can be conceptualized to be derived from topochemical deintercalation of lithium from δ-$Li_xV_2O_5$ ($0.88 < x < 1.0$).[112] The overall lamellar structures of α-V_2O_5 and δ-V_2O_5 are similar; however, the alternate sheets are shifted from each other by half a unit cell in the *c* direction (Figure 4C). The γ'-V_2O_5 phase can be derived from δ-V_2O_5 by rotation of the two edge-shared $[VO_5]$ pyramidal units by 90° in opposite directions along V1−O1 and V2−O2, respectively, as

Table 1. Calculated Open-Circuit Voltages (OCVs) for Li- and Mg-Ion Intercalation in Several Polymorphs of V_2O_5[a]

	OCV-Li (V)	OCV-Mg (V)	E_{hull}-V_2O_5 (meV)	E_{hull}-$Li_xV_2O_5$ (meV)	E_{hull}-$Mg_xV_2O_5$ (meV)	Li-ion diffusion barrier (eV)	Mg-ion diffusion barrier (eV)	change in oxygen coordination environment
α-V_2O_5	3.35	2.59	0	45	118	0.11−0.16	1.15−1.23	8→3→8
γ'-V_2O_5	3.44	2.73	6	27	50	0.18−0.15	0.71−1.16	4→3→5→3→4
ζ-V_2O_5	3.71	3.28	24	23	−17	0.13−0.14	0.62−0.86	4→3→5→3→4
ρ'-V_2O_5	3.74	2.86	30	38	85	0.07−0.07	0.28−0.46	4→3→5→3→4
δ'-V_2O_5	3.59	2.80	32	53	149	0.07−0.19	0.54−1.07	4→3→5→3→4
ε'-V_2O_5	3.72	2.92	32	47	83	0.10−0.11	0.21−0.24	4→4→4→4→4

[a] Energy-above-hull (E_{hull}), which predicts the stability of the polymorphs with respect to their stable constituents in meV/atom, is also noted. An E_{hull} value of 0 meV/atom represents the polymorph that is the ground state of the system. Migration energy barriers in electronvolts per unit supercell and the change in oxygen coordination environment for Li- and Mg-ions are also noted for each polymorph.

shown in Figure 4D. This puckering occurs only along alternate [VO_5] pairs of the lamellar sheet. As a result, the apical V═O bonds are slightly skewed along the crystallographic *b* axis, in contrast with α-V_2O_5 and δ-V_2O_5, where they all point in the same direction. In contrast, ρ'-V_2O_5, δ'-V_2O_5, and ε'-V_2O_5 comprise double-layered V_4O_{10} units sharing corners and edges, which are held together by van der Waals forces along the crystallographic *c* direction. Notably, these three double-layered polymorphs differ from each other in terms of stacking of the V_4O_{10} double layers along the *a* direction. The δ'-V_2O_5 and ε'-V_2O_5 polymorphs can be derived from the ρ'-V_2O_5 phase by sliding of the alternate double layers along the crystallographic *a* direction (Figure 4F−H). β-V_2O_5, a high-pressure phase with a space group symmetry of $P2_1/m$,[70] comprises two [VO_6] units that share an edge to form a double-layered unit; these units share corners in the *a* and *b* crystallographic direction to form a double-layered 2D sheet (Figure 4E). The structure can be conceptualized to result from the parent α-V_2O_5 phase by bringing the layers together along the *c* axis and sliding along the direction delineated by arrows in Figure 4E. The metastable phase ζ-V_2O_5 is distinct in adopting a 1D tunnel structure with a space group symmetry of $C2/m$.[74,107] It comprises three distinct vanadium centers: (a) distorted $V(1)O_6$ octahedra connected at edges, (b) distorted $V(2)O_6$ octahedra connected at corners, and (c) $V(3)O_5$ pentagonal square pyramids. This phase can be related to the δ'-phase through several slip, condensation, and distortion processes, and indeed the reversible interconversion of Ca-intercalated frameworks β-$Ca_xV_2O_5$ to δ-$Ca_xV_2O_5$ has been experimentally realized.[113]

5.3.2. Calculated Thermodynamic and Kinetic Parameters. The fundamental cell voltage of a battery is derived from the difference in chemical potential between the anode and cathode selected for the cell, which, in turn, is dependent on the change in Gibbs free energy between the charged and discharged states. As such, varying the framework connectivity via selection of polymorph (by selection of metastable materials) can serve as a handle to tune the electrochemical potential of one-half of the cell and thus the voltage of the entire cell, all without changing composition. The average open-circuit voltages for Li-ion and Mg-ion in various polymorphs of V_2O_5 calculated using DFT are contrasted for different polymorphs of V_2O_5 in Table 1.[74,75,92] The voltages are computed with respect to the bulk metal anode (body-centered Li and hexagonal close-packed Mg) in each case.[73,92,114,115] Two main inferences can be drawn from the computed voltages. First, the open-circuit voltages (OCVs) follow the same trend as the standard reduction potential in the aqueous electrochemical series (−3.04 V vs SHE for Li and −2.37 V for Mg). Second, the OCVs for the cation intercalated metastable phases of V_2O_5 are higher in comparison with α-V_2O_5. The primary origin of the higher voltages is the relative instability of the metastable polymorphs in comparison with α-V_2O_5. As shown in Table 1, metastable phases γ'-V_2O_5, ζ-V_2O_5, ρ'-V_2O_5, δ'-V_2O_5, and ε'-V_2O_5 are 6, 24, 30, 32, and 32 meV per V_2O_5 unit unstable in energy than α-V_2O_5. The intercalated phases of α-V_2O_5 are relatively more stable than intercalated phases of metastable V_2O_5. However, the difference in energy between the intercalated metastable phases and its discharged phase is higher in comparison with the same differential in energy for α-V_2O_5.

The stability of the cathode further represents an important parameter. Table 1 plots the energy of decomposition (E^{hull}) for different polymorphs. A cathode material with an E^{hull} value of zero is considered to be thermodynamically stable, whereas a positive E^{hull} value suggests instability. α-V_2O_5 is considered to be the thermodynamic sink with a E^{hull} value of zero. In contrast, γ'-V_2O_5, ζ-V_2O_5, ρ'-V_2O_5, δ'-V_2O_5, and ε'-V_2O_5 are only 6, 24, 30, 32, and 32 meV higher in energy, respectively, suggesting the potential accessibility of several energetically proximate polymorphs close at room temperature. Similarly, α-LiV_2O_5, γ-LiV_2O_5, β'-$Li_{0.66}V_2O_5$, ρ-$Li_{0.5}V_2O_5$, δ-LiV_2O_5, and ε-LiV_2O_5 are 45, 27, 23, 38, 53, and 47 meV higher in energy, suggesting their potential viability. However, α-MgV_2O_5 and δ-MgV_2O_5 are highly unstable with high E^{hull} values of 118 and 149 meV, suggesting that these phases are unlikely to be good intercalation hosts. Remarkably, β-$Mg_{0.33}V_2O_5$ is −17 meV more stable and γ-MgV_2O_5, ρ-$Mg_{0.5}V_2O_5$, and ε-MgV_2O_5 are only 50, 85, and 83 meV above the thermodynamic stable state, suggesting that they might be readily accessible at room temperature. In general, double-layered and tunneled-structured V_2O_5 phases appear to be much more stable as compared with single-layered V_2O_5.

The migration energy barrier (E_b) is defined as the maximum energy required for an intercalant to hop between two low-energy-lying intercalant positions through the transition-state geometry. To provide a perspective of the numerical values, a 60 meV change in barrier energy is enough to change the diffusivity of the intercalants by one order of magnitude. For a micrometer-sized particle to be used as a viable cathode material, diffusion barriers <0.525 eV have been suggested, whereas for nanometer-sized particles, slightly higher diffusion barriers on the order of 0.650 eV can be tolerated given the shorter diffusion path lengths.[116] The computed diffusion barriers for Li-ions are low for all of the polymorphs, translating to an approximate diffusivity of (2 to 4) × 10^{-4} cm^2 s^{-1}. For Mg-ions, the migration barrier is 1.15 to 1.23 eV in α-V_2O_5, which decreases to ca. 0.71 to 1.16 eV in γ'-V_2O_5, ca. 0.62 to 0.86 eV in ζ-V_2O_5, 0.28 to 0.46 eV in ρ'-V_2O_5, 0.54 to 1.07 eV in δ'-V_2O_5, and ca. 0.21 to 0.24 eV in ε'-V_2O_5. The computed barrier for Mg-ions at the initial charging limit in all of the metastable polymorphs

DOI: 10.1021/acs.jpcc.8b04622
J. Phys. Chem. C XXXX, XXX, XXX−XXX

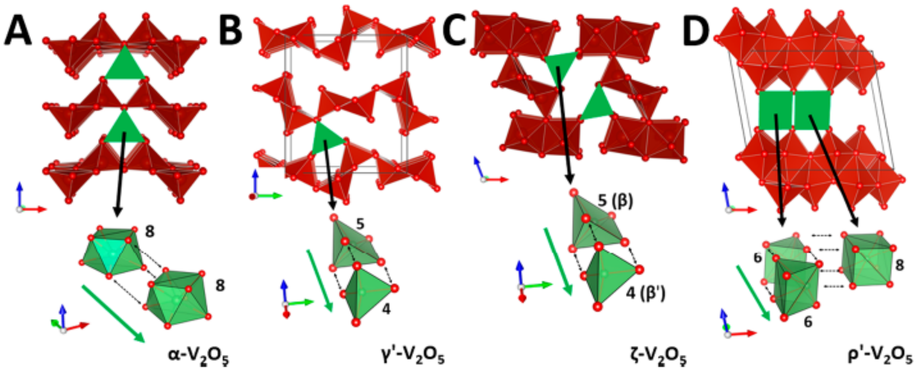

Figure 5. Cation-oxygen coordination environment during mono/multivalent ion diffusion in (A) thermodynamically stable phase α-V_2O_5 and metastable phases, (B) γ'-V_2O_5, (C) ζ-V_2O_5, and (D) ρ'-V_2O_5. The green arrow shows the lowest energy pathway for diffusion, and the numbers indicate the change in the coordination number during the process of diffusion. Parts of this Figure are reproduced with permission from refs 73 and 75. Copyright 2018 Elsevier and 2017 American Chemical Society.

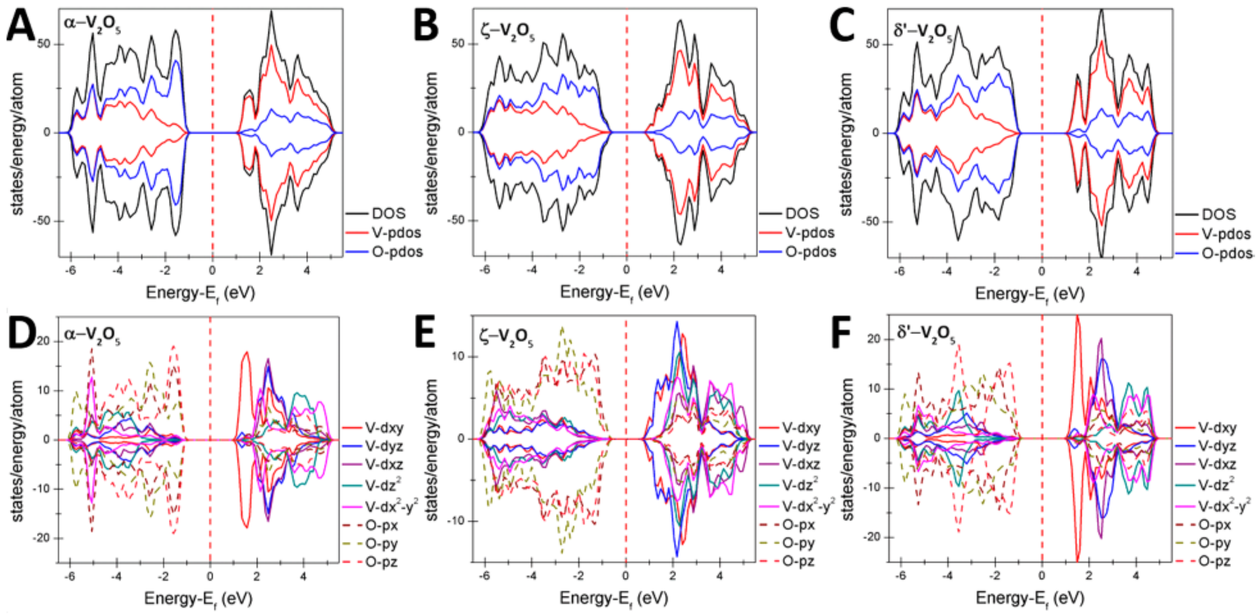

Figure 6. (A−C) Total density of states and atom-projected density of states. Vanadium and oxygen orbital-projected density of states for (D) α-V_2O_5, (E) ζ-V_2O_5, and (F) δ'-V_2O_5.

(except γ'-V_2O_5) is around or below 650 meV, suggesting their viability as cathode materials.

5.3.3. Cation Diffusion Pathways in V_2O_5 Polymorphs. Table 1 indicates that minor changes in coordination framework of the polymorphs can give rise to substantial changes in the diffusion barrier.[72] Figure 5 illustrates the change in the local coordination environment of intercalated cations in four polymorphs of V_2O_5, namely, α-V_2O_5, γ'-V_2O_5, ζ-V_2O_5, and ρ'-V_2O_5. In α-V_2O_5, the migration of the intercalating cation occurs across the layers of staggered 1D chains of oxygen atoms along the crystallographic *b* direction. Notably, the change in coordination environment is 8 → 3 → 8 along oxygen coordinated sites with the cation resident in a trigonal planar environment in its transition state.[74,117] The large diffusion barrier can be attributed to the large change in coordination number and suboptimal coordination environment of the cation in the spatially constrained transition state. In contrast, several of the metastable polymorphs offer much more spacious transition states, and cation diffusion is accompanied by smaller alterations of coordination number, as illustrated in Figure 3 and delineated in Table 1, giving rise to substantially lower diffusion barriers. A major advantage of metastable compounds is thus the ability to access a variety of conduction pathways for intercalated ions, which can substantially alter the kinetics of diffusion.

5.4. Electronic Structure Differences between V_2O_5 Polymorphs. The varying V−O connectivity profoundly changes the electronic structure of V_2O_5 polymorphs; altering the energy dispersion of conduction band states and varying the band gap provides a means to tune electron transport and further makes available a variety of semiconductors with tunable separations between valence and conduction band edges. The electronic structure of the polymorphs has substantial implications for intercalation chemistry given the oftentimes coupled nature of electron and ion diffusion (observed by the creation of small polarons and the self-trapping of small polarons by Li-ions).[108,118]

In α-V_2O_5, the localization of electrons on V $3d_{xy}$ orbitals and the subsequent structural relaxation of the V−O lattice phonon mode upon lithiation create a small polaron that traps the diffusing Li ions and hampers their facile diffusion.[119] There is a growing realization that the electronic structure plays an important role in the electronically coupled diffusion of a cation through the lattice.[92,108,120] Figure 6 contrasts the total density of states (DOS) and the atom-projected density of states (PDOS) of several selected polymorphs of V_2O_5, illustrating the substantial implications of altered atomistic connectivity on the electronic structure. In all depicted polymorphs of V_2O_5, the valence band is predominantly derived from O 2p states, whereas the conduction band is primarily vanadium 3d in origin.[121,122] On careful observation, the conduction band can be roughly separated into t_{2g} and e_g states. The lower energy t_{2g} states correspond to V $3d_{xy}$, $3d_{xz}$, and $3d_{yz}$ orbitals engaged in π-overlap with O 2p orbitals, whereas higher energy e_g states have contributions from V $3d_{z^2}$ and $3d_{x^2-y^2}$ engaged in head-on σ-overlap with O 2p orbitals. In α-V_2O_5, owing to the distortion of the vanadium coordination from a perfect octahedron, a nonbonding split-off band V $3d_{xy}$ band is formed below the rest of the conduction band. Early transition metals tend to have narrow 3d bands, as is the case in V_2O_5.[71,73,108] The localization of charge in such narrow bands has a deleterious influence on electronic transport properties and further impedes ion transport through self-trapping of ions by small polarons.[71,118] In sharp contrast, ζ-V_2O_5 crystallizes in a lower symmetry structure with reduced structural dimensionality and has three distinct vanadium-centered polyhedra (two crystallographically inequivalent octahedra and one square pyramid). In ζ-V_2O_5, degenerate V $3d_{xy}$ and V $3d_{yz}$ orbital character is observed at the conduction band edge (Figure 6B). The broader energy dispersion of bands and the inclusion of the previously split-off states within the conduction band yield a lower band gap polymorph with considerably greater covalent character of V−O bonds; as such, it substantially mitigates polaronic self-trapping,[71,73] which is evidenced experimentally by the improved Li- as well as Mg-ion diffusion in ζ-V_2O_5[73,92] as compared with α-V_2O_5.[104,123] Unlike α-V_2O_5, which undergoes several phase transitions upon lithiation as a result of gaps in miscibility,[104,108] the rigid 3D tunnel-structured framework is preserved across a wide range of Li- and Mg-ion insertion in ζ-V_2O_5,[73,107] yielding a large solid solution range with minimal volume expansion (<2%).[73,74]

Similar to the α-V_2O_5 structure, the double-layered δ'-V_2O_5 phase (and similar polymorphs such as ε'-V_2O_5 and ρ'-V_2O_5) has a sharp split-off conduction band that is primarily V $3d_{xy}$ in origin (Figure 6C).[71] The presence of split-off band, despite having two nonequivalent V sites, suggests the possibility of periodic charge ordering when the structure is distorted. As a result of stronger V═O bonding in the double-layered frameworks, δ'-V_2O_5 further shows increased covalency of V−O connectivity, which reduces the extent to which the intercalated cations are bonded to the anionic framework. It is clear from this limited comparison that the electronic structure of V_2O_5 polymorphs is delicately sensitive to the connectivity of V−O polymorphs, allowing for considerable tunability of effective orbital overlap and thus ionic/covalent character.

As detailed in recent work examining the mechanism of Mg-ion diffusion within ζ-V_2O_5,[73] ionic diffusion of the inserted cation and electronic diffusion of the localized electron/phonon (polaron) pair are inextricably coupled.[73] Importantly, the energetic barrier arising from this concerted diffusion is exacerbated when considering the diffusion of divalent cations, which requires the concomitant diffusion of two polarons. Perhaps a more compelling and broad conclusion that emerges is that when designing multivalent-ion cathode materials, consideration of ionic diffusion alone is insufficient.[72] Additional attention to mitigating small polaron formation and the resulting self-trapping of intercalated cations is of great importance, particularly in early first-row transition metals with narrow 3d bands. Careful selection of metastable polymorphs allows for considerable tunability of electronic structure and by means of the available bonding motifs provides a valuable tool for potentially mitigating such problems. In other words, metastable materials provide opportunities to modulate the electronic structure and relative ionicity/covalency of cathode materials (in addition to defining different diffusion pathways),[72] which can greatly modify interactions with intercalated cations.

6. SIZE-DEPENDENT PHASE DIAGRAMS OF TRANSITION-METAL OXIDES: COMPARING AND CONTRASTING HfO_2 AND ZrO_2

Scaling materials to nanoscale dimensions holds opportunities for modifying phase diagrams and accessing metastable polymorphs; the size dependence of relative phase stabilities is derived from the increased importance of surface free-energy terms at these dimensions. At nanoscale dimensions, surface free-energy terms, scaling as a function of surface area, can counteract bulk free-energy differentials and enable the stabilization of unusual structural motifs.[4,124−126] These conditions thereby correspond to constrained equilibrium rather than kinetic trapping. In other words, size can be considered to be an axis along a free-energy landscape, such as plotted in Figure 1, wherein the relative stabilities of different polymorphs are altered. The stabilization of the tetragonal polymorph of HfO_2 is of immense technological importance given the predicted high dielectric constant of this phase[78,127] but has proven to be much more synthetically challenging in comparison with the stabilization of tetragonal ZrO_2, which is structurally similar and is characterized by an analogous sequence of phase transformations. Indeed, HfO_2 and ZrO_2 are often denoted as “twin metal oxides” given the close parallels in their chemical reactivities and physical properties. The similarities between the two metal oxides derive from the almost identical ionic radii of tetravalent hafnium (0.78 Å) and zirconium ions (0.79 Å), which is a result of lanthanide contraction.[128] However, whereas the tetragonal phase of ZrO_2 can be readily accessed below a critical size of 30 nm,[41,51,129] the stabilization of tetragonal HfO_2 has proven to be a considerably greater synthetic challenge.[53,54]

6.1. HfO_2 Polymorphs, their Crystallographic Relationships, and Comparisons to ZrO_2. At room temperature, bulk HfO_2 crystallizes in a monoclinic ($P2_1/c$) lattice.[130] With increasing temperature (variously pegged at 1670—1720 °C for HfO_2), a Martensitic phase transformation from the monoclinic to the tetragonal ($P4_2/nmc$) phase is observed. A further increase in temperature to ca. 2200 °C brings about a diffusionless tetragonal → cubic ($Fm\bar{3}m$) phase transformation; the cubic structure is retained until HfO_2 is congruently melted at 2810 °C.[128,131,132] Unit cells for these three thermally accessible phases of HfO_2 are depicted in Figure 7. Video 1 depicts the sequence of atomic displacements that bring about the phase transformations. The monoclinic crystal structure of HfO_2 is characterized by tetravalent hafnium-cations ensconced within seven-coordinated sites. The monoclinic to tetragonal phase transition involves a 9° shear of the unit cell and a volume expansion of 2.7% for HfO_2 (compared to ca. 4.5%[125] for ZrO_2).[133,134] Both phases further have a number of twin variants allowing for manifestation of ferroelastic domains that can further self-organize into periodic patterns upon dimensional confinement or strain.[135−137]

In the tetragonal unit cell of HfO_2 (and ZrO_2), the tetravalent metal ions are ensconced within eight-coordinated environments comprising four oxygen atoms in close proximity to the

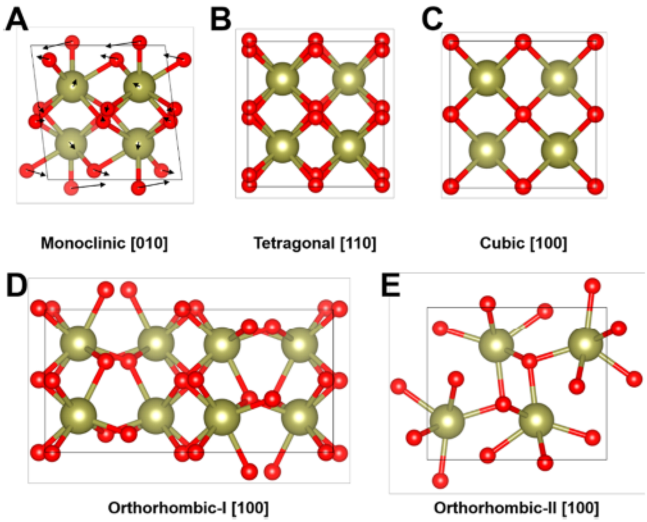

Monoclinic [010] Tetragonal [110] Cubic [100]

Orthorhombic-I [100] Orthorhombic-II [100]

Figure 7. Unit cells of (A) monoclinic, (B) tetragonal, (C) cubic, (D) orthorhombic-I, and (E) orthorhombic-II phases of HfO_2. The arrows in panel A depict the atomic displacements necessary to transform to the tetragonal phase in panel B. Hafnium atoms are represented as gold spheres, whereas oxygen atoms are shown as red spheres (see also Video 1).

metal atom at a separation of 2.09 Å and four atoms slightly further away at a distance of 2.31 Å, defining two distinct tetrahedra around the metal atom. During the symmetry-raising monoclinic → tetragonal phase transition, the oxide ions are displaced along the (001) direction as a result of close O—O contacts, creating a tetragonal distortion[78] with a c/a ratio of 1.025.[138]

The stabilization of tetragonal HfO_2 has proven to be a much greater synthetic challenge owing to the increased differential in thermodynamic stabilization between the monoclinic and tetragonal phases, as depicted in Table 2 (the tetragonal phase of ZrO_2 is stabilized at 1170 °C, whereas stabilization of tetragonal HfO_2 requires temperatures of 1680—1720 °C).[128,139] The differential in bulk free energy between the monoclinic and tetragonal phases is estimated to be 196 meV for HfO_2 as compared with 140 meV for ZrO_2. The smaller volume expansion for HfO_2 also brings about a more facile reversion to the monoclinic phase upon cooling, which further renders kinetic trapping of the metastable polymorph more difficult.[135]

The eight-coordinate cubic $Fm\bar{3}m$ phase of ZrO_2 has a unit-cell parameter of 5.15 Å and has not thus far been stabilized at room temperature without the incorporation of dopant atoms. Cubic ZrO_2 (and for that matter HfO_2) can be stabilized at room temperature through aliovalent incorporation of divalent or trivalent dopants such as Y^{3+}, Sc^{3+}, V^{3+}, and Ca^{2+}. These dopants introduce oxygen vacancies, which thereby allow for Zr atoms to be seven-coordinated while allowing for crystallization in a higher symmetry cubic space group on average.[143,144] Indeed, cubic ZrO_2 incorporating aliovalent dopants such as Y^{3+}, Sc^{3+}, or Ca^{2+} is known to be an excellent solid-state electrolyte at high temperatures owing to the facile diffusion of oxygen vacancies.

Analogous to the temperature-variant phase stability diagram, a pressure-variant phase diagram can be mapped and indeed yields two noncentrosymmetric oxygen-deficient orthorhombic phases of HfO_2 (and ZrO_2). An orthorhombic-I (O1, space group *Pbca*) is stabilized above 4.3 GPa, and an orthorhombic-II (O2, space group *Pnma*) phase is stabilized at a pressure above 14.5 GPa (Figure 7D,E).[63,145] These pressure-induced transformations are also theorized to be diffusionless transitions and result from displacive unit-cell distortions.[54,139,146]

6.2. Implications of Polymorphism for Functional Properties. The rich phase diagrams of HfO_2 and ZrO_2, tunable as a function of temperature, pressure, and point defects, along with the facile accessibility of several polar variants for the low-symmetry polymorphs, have inspired extensive investigations of the properties of these materials. Two important implications of this rich phase diagram are transformation toughening and shape memory behavior, which hold promise for realizing unprecedented mechanical properties in ceramic materials that tend to otherwise be rather brittle. Because ferroelastic properties have been observed in the monoclinic structure of ZrO_2 as a result of the stabilization of nanotwinned domains, it has been posited that the tetragonal structure may display superelastic properties.[147] Upon application of stress to the tetragonal structure, it undergoes a phase change to the monoclinic structure, followed by domain switching through ferroelastic domain wall movement, thereby allowing for multiple means of energy dissipation before plastic deformation.

In addition, considerable attention has focused on the utilization of the high dielectric constant of HfO_2 polymorphs stemming from their soft phonon modes and high Born effective charge tensors.[78] The phonon dispersion and extent of covalency of metal—oxygen bonds are determined by the metal—oxygen connectivity in HfO_2 and ZrO_2, which thus plays an important role in determining the dielectric constant. As noted above, first-principles calculations predict a dielectric constant of 70 for tetragonal HfO_2[78] in comparison with 18 for the thermodynamically stable monoclinic phase.[148] The interest in new dielectric materials arises from the fundamental limitations of SiO_2 dielectrics. Whereas SiO_2 dielectrics are entirely compatible with Si active elements, SiO_2 has a dielectric constant of only ca. 3.5.[149] Because C varies with the area (A), thickness (d), and dielectric strength (k) as $C = kA/d$ to preserve the same value of capacitance while aggressively scaling areal dimensions of the device, the dielectric constant must be increased or the thickness of the dielectric layer has to be decreased. The latter approach is severely constrained by enhanced leakage currents that result in increased power consumption. Consequently, higher dielectric constant materials have emerged as an urgent imperative, and indeed the development of amorphous HfO_2 dielectrics and their integration onto Si mark a key milestone that has enabled the continued scaling of device dimensions.[78,149] The high predicted dielectric constant of the tetragonal phase of HfO_2

Table 2. Calculated Differentials in Bulk and Surface Energies between the Monoclinic and Tetragonal Phases of HfO_2 and ZrO_2[140a]

oxide	tetragonal→monoclinic transition temperature (°C)	volume expansion (%)	difference in surface energy between monoclinic and tetragonal phases (mJ/m^2) ($\Delta U_{surface,monoclinic} - \Delta U_{surface,tetragonal}$)	difference in bulk energy between monoclinic and tetragonal phases (meV) ($\Delta G_{bulk,monoclinic} - \Delta G_{bulk,tetragonal}$)
HfO_2	1680[128,139,141]	2.7[133,134]	−246[140]	196[140]
ZrO_2	1170[128,139]	ca. 4.0[142]	−225[140]	140[140]

[a] Data reprinted with permission from ref 135. Copyright 2014 American Chemical Society.

holds tantalizing promise for further reducing power consumption in electronic devices, but rather inconveniently, this phase is a high-temperature phase stable only above 1670 °C in the bulk.

The orthorhombic phases of HfO_2 and ZrO_2 (Figure 7D,E) have attracted considerable interest owing to the recent observed manifestation of ferroelectricity in these binary oxides.[136] Because such materials can be accessed by modifications to well-established atomic layer deposition methods, they hold great promise for the realization of novel devices such as neuromorphic memresistors underpinned by switching between energetically proximate metastable polymorphs. In addition to pressure, such phases can be stabilized in thin film form using strain effects as well as through the incorporation of dopants.[63,64,150] Indeed, the utilization of high-throughput first-principles DFT calculations to examine the influence of different dopants on the Hf–O phase diagram represents an excellent example of a computationally guided exploration targeting stabilization of a metastable polymorph.[63,64,150]

6.3. Stabilizing Tetragonal HfO_2 through Dimensional Confinement. Despite the rich phase diagrams of HfO_2 and ZrO_2, the high temperatures have thus far precluded detailed experimental evaluation of the mechanisms underpinning the phase transitions. Most of the available information is derived from theoretical calculations of deformations, bond stretching, and putative displacement pathways that, however, remain to be experimentally validated (or refuted).[126,151] One mechanism for stabilizing tetragonal HfO_2 well below its equilibrium transition temperature of 1670 °C involves modification of the transformation mechanism through nucleation of the phase transition at a coherent twin boundary. Indeed, we have observed that (100) coherent twin boundaries (Figure 8) are stabilized across monoclinic 1D HfO_2 nanorods grown by the condensation of $HfCl_4$ and $Hf(O^tBu)_4$; these twin defects are thought to form to alleviate strain within the crystallite upon cooling from an incipient tetragonal phase to the monoclinic phase that is stabilized at room temperature.[135] To alleviate strain generated upon volume expansion during the phase transformation, deformation and spontaneous organization of twin boundaries are observed along the length of the crystal. Figure 8 depicts the ferroelastic organization of twinned domains that are seen to form "bar-code" like patterns spanning the entire diameter of a nanorod.

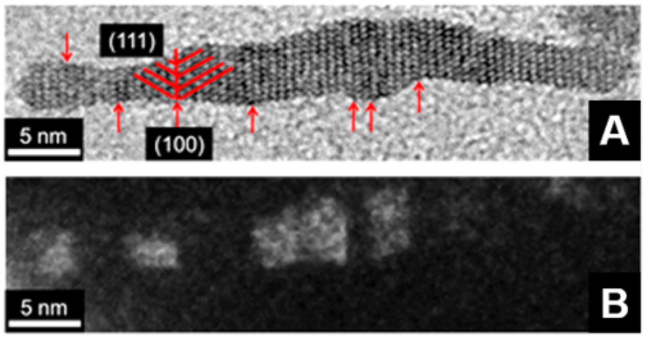

Figure 8. (A) Lattice-resolved HRTEM image of an individual HfO_2 nanorod. Arrows indicate the (100) twin planes. Red lines highlight the (111) lattice fringes as they cross the twin plane. (B) Dark-field TEM image of panel A constructed using the (111) diffraction spot. Reprinted with permission from ref 135. Copyright 2014 American Chemical Society.

The phase evolution of these nanorods upon heating has been examined using in situ high-angle annular dark field scanning transmission electron microscopy (HAADF STEM) measurements.[54] Remarkably, Figure 9 indicates that at a temperature of 600 °C, the nucleation of a tetragonal domain is observed at a twin boundary, depressed by >1000 °C from the bulk transition temperature.[135] The sequence of images in Figure 9 further indicates the propagation of a transformation dislocation across the nanorod, with conservation of a one-to-one lattice correspondence across a phase boundary; the nanorod is entirely transformed to the tetragonal phase after 60 min. The thermodynamic underpinnings of the depression of the phase transformation temperature are discussed in a subsequent section, but clearly extended defects and size combine in this case to facilitate the stabilization of the tetragonal polymorph at a much lower temperature as compared with the bulk.

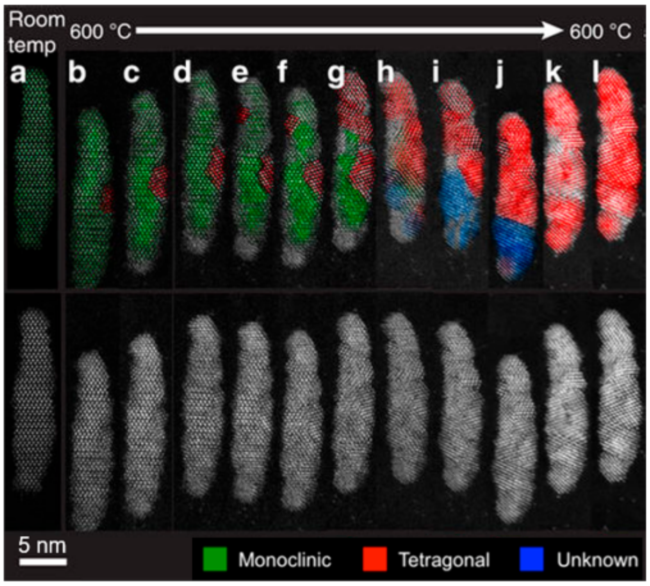

Figure 9. False-colored HAADF STEM images highlighting the structural phases present in each frame. (a) Before annealing, the nanorod is monoclinic. (b–l) Over a period of ∼40 min the nanowire converts completely from single-crystalline twinned monoclinic to polycrystalline tetragonal hafnia with retention of the overall morphology. Reprinted with permission from ref 54. Copyright 2017 Nature Publishing Group.

As noted above, conventional ceramic processing routes impart an excess of energy to a material, thereby enabling it to descend toward equilibrium along a free-energy landscape (such as plotted in Figure 1) without being trapped in metastable states. In contrast, solution-phase synthesis routes have the potential to carefully "deposit" the material in a local minimum based on structural similarities with precursors and specific peculiarities of the nucleation and growth process. Establishing dimensional confinement utilizing solution-phase colloidal synthesis provides a means to access specific parts of the energy landscape without a large excess of energy. In colloidal nanoparticle synthesis, kinetic parameters can be controlled by temperature and precursor diffusion coefficients and by matching precursor reactivities. Rapid crystallization methods can be used to promote the stabilization of metastable structures (avoiding very high supersaturation, which oftentimes yields amorphous products). Slower crystallization, in turn, enables precise control of nanocrystal size.

DOI: 10.1021/acs.jpcc.8b04622
J. Phys. Chem. C XXXX, XXX, XXX−XXX

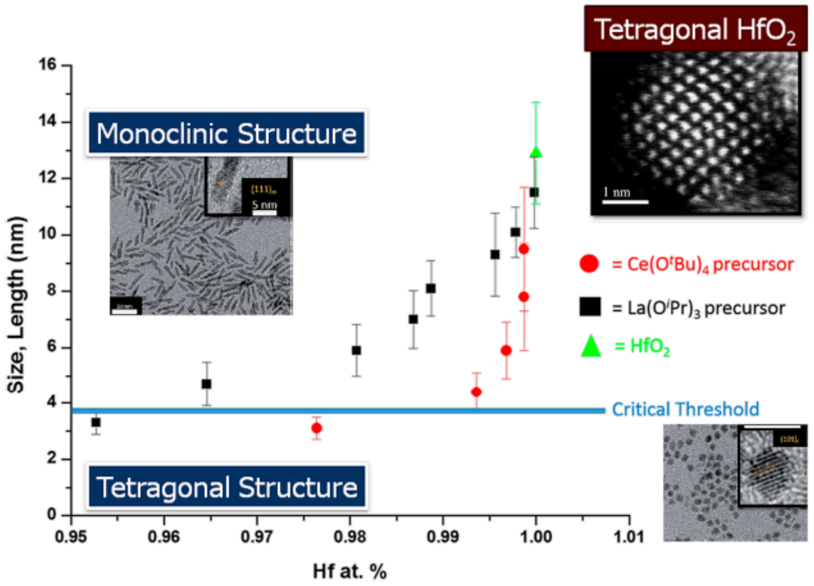

Figure 10. Size dependence of crystal structure of HfO_2 nanocrystals prepared by a nonhydrolytic condensation approach. The tetragonal phase of HfO_2 is stabilized below a critical size of 3.6 to 3.8 nm. The top right inset depicts an atomically resolved electron microscopy image of an individual tetragonal HfO_2 particle, whereas the top left and bottom right insets depict HRTEM images of monoclinic and tetragonal HfO_2 nanocrystals, respectively. Reprinted and adapted with permission from ref 53. Copyright 2016 The Royal Society of Chemistry.

Nonhydrolytic sol—gel syntheses represent a useful palette of "soft chemistry" synthetic routes and have afforded considerable control over particle size and composition, allowing for the synthesis of well-defined HfO_2, ZrO_2, as well as solid-solution $Hf_xZr_{1-x}O_2$ nanocrystals.[128,131,152] In this approach, oxo linkages are created as a result of the condensation reaction between a metal halide and a metal alkoxide with the elimination of an alkyl halide as per[128,131,152,153]

$$\equiv M{-}X + \equiv M{-}O{-}R \rightarrow \equiv M{-}O{-}M\equiv + R{-}X \tag{2}$$

The condensation reaction is believed to involve coordination of the metal center of the halide to the oxygen atom of the metal alkoxide, followed by nucleophilic attack of the R-group by the halide and the elimination of an alkyl halide in an $S_N{}^1$-type fashion.[49,154,155] Typically tri-*n*-octylphosphine oxide (TOPO) is used as the surface-passivating ligand for obtaining nanocrystals that are monodisperse, although recent ^{31}P nuclear magnetic resonance studies suggest that the protonated form of TOPO, hydroxyl-tri-*n*-octylphosphonium, $[HO\text{-}PR_3]^+$, is tightly bound to the nanocrystal surfaces along with di-*n*-octylphosphinate and *P*,*P*′-(di-*n*-octyl) pyrophosphonate.[156] Recognizing that the condensation reaction proceeds through an $S_N{}^1$ mechanism, the electronic and steric substituent effects of the alkyl chain of the alkoxide precursor are seen to have a significant influence on the reactivity of the precursor in the condensation reaction and can thus substantially impact the kinetics of crystal growth, the eventual morphology, and even the crystal structure of the nanocrystalline products.[135,152] When two different metal precursors are reacted, the condensation rate is strongly influenced by the reactivity of each precursor, which allows for substantial control over the relative stoichiometry of metals incorporated within solid-solution products of a heterocondensation reaction[128,139]

$$mMX_n + nM'(OR)_m \rightarrow M_mM'_nO_{nm} + nmRX \tag{3}$$

The incorporation of a less reactive precursor (e.g., $Ce(O^tBu)_4$ or $La(O^iPr)_3$) in conjunction with $HfCl_4$ and $Hf(O^tBu)_4$ greatly retards the kinetics of the homocondensation reaction. Constraining the growth kinetics yields HfO_2 nanocrystals with ultrasmall dimensions, thereby enabling a detailed evaluation of the size dependence of the phase diagram of HfO_2. Figure 10 indicates that the critical size for stabilization of tetragonal HfO_2 is ca. 3.6 nm, substantially reduced from the 30 nm threshold value generally stated for ZrO_2.[53] In other words, by providing access to monodisperse nanocrystals with tunable dimensions, this synthetic approach provides a means to systematically evaluate the balance between surface energy and bulk free energy as a function of particle size. At ultrasmall dimensions, the tetragonal phase of HfO_2 can thus indeed be stabilized under ambient temperature and pressure conditions.

6.4. Account of Thermodynamic Considerations Determining Phase Stabilization in HfO_2. It was in 1965 that Garvie and coworkers first reported that the tetragonal phase of ZrO_2 can be stabilized below a certain critical particle size (variously estimated to be 15—30 nm) as a result of surface energy considerations.[4,51,141,157] Table 2 shows that the monoclinic phase of ZrO_2 is 5.5 kJ/mol more stable in terms of bulk enthalpy as compared with the tetragonal phase; however, the surface energy of the tetragonal phase is 225 mJ/m^2 lower than that of the monoclinic phase.[4,140,157] Below a critical size, the tetragonal phase is thus stabilized at room temperature as a result of increased surface energy contributions. Examples of the stabilization of tetragonal ZrO_2 have been well documented for bulk ceramics and thin films; however, the stabilization of tetragonal HfO_2 has proven to be much more difficult.[134,140,141] The primary origin of this challenge is the greater differential of bulk free energies (ΔG), almost 40% greater for HfO_2 as compared with ZrO_2 (Table 2).[134,140,141] A full account of the different energy terms involved in the phase transformation is warranted to understand the pronounced size dependence of the phase stability. The change in free energy for a monoclinic—tetragonal transformation can be separated into the following components[158]

$$\Delta G_{M\rightarrow T} = G_M^c - G_T^c + U_{SE}^M - U_{SE}^T + U_S^M - U_S^T \tag{4}$$

where G^c is the chemical free energy, U_{SE} represents the strain energy, U_S is the surface energy, and the superscripts M and T denote the tetragonal and monoclinic phases, respectively.[159] At room temperature, the ΔG^c value will be strongly positive given the 196 meV differential (Table 2), which favors retention of the thermodynamically stable monoclinic phase. Indeed, even at a temperature of 600 °C, the ΔG^c value will be strongly positive in the bulk, favoring retention of the monoclinic phase. Nevertheless, it is clear from Figure 9 that $\Delta G_{M\rightarrow T} \leq 0$ at 600 °C for the twinned nanorods given the observation of a monoclinic → tetragonal transition; indeed, this implies that the surface and strain energy differentials must be of a sufficient magnitude to overcome the highly positive chemical free-energy differential. It is these two parameters that thus underpin suppression of the transition temperature by almost 1000 °C. The ΔU_S surface energy term can be written for a spherical particle as

$$\Delta U_S^{M\rightarrow T} = \frac{6(\gamma_T - g_s\gamma_M)}{D} \tag{5}$$

where the γ terms represent the interfacial surface energies, D is the diameter of the particle, and $g_s = A_M/A_T$, which describes the ratio of the interfacial surface areas.[51] Equation 5 describes the pronounced size dependence of the surface energy term and shows that the smaller the size of the particle, the higher the numerical value of the surface energy differential. The specific numerical values of the γ terms will influence the sign of the $\Delta U_S^{M\rightarrow T}$ term. Ramprasad and coworkers have shown from first-principles DFT calculations that the surface energies of the lowest-energy (110) and (001) lattice planes of HfO_2 govern the relative phase stabilities at finite dimensions. Calculated values for (110) and (001) planes of monoclinic HfO_2 are 1.38 and 1.51 J m^{-2}, respectively, whereas the corresponding values for the tetragonal planes are 1.08 and 1.21 J m^{-2}, respectively. As a result, the $\Delta U_S^{M\rightarrow T}$ term is negative, with the diameter serving as a weighting factor.[126] This analysis thus illustrates the key role of particle size in counteracting the strongly positive ΔG^c value and indeed is the origin of the stabilization of the tetragonal phase at room temperature upon scaling to ultrasmall dimensions evidenced in Figure 10.

The second term that impacts the transition temperature is the ΔU_{SE} strain energy term. This term can be attributed to the twin planes of the nanorods, where in Figure 8 the compensation of the transformation strain across the nanorod is alleviated by the plastic deformation induced by the twin planes during synthesis. The energy stored within the twin planes is dissipated during the transformation from monoclinic to tetragonal, thus implying $\Delta U_{SE}^{M\rightarrow T} < 0$, further working in the opposite direction from the positive ΔG^c differential imposed by the bulk free energy. Lange and coworkers have deduced a size-dependent expression for twin boundaries as per[159]

$$\Delta U_{SE}^{M\rightarrow T} = -\frac{6\gamma_{twin}g_{twin}}{D} \tag{6}$$

where γ_{twin} is the twinning energy per unit area and g_{twin} is a dimensionless quantity expressed as $\frac{A_{twin}}{\pi D^2}$, where A_{twin} is the total area of the twin boundaries. As seen in Figure 9, the twin planes serve as a nucleation point within the nanorod, which corresponds to a high-energy region of the energy landscape. A high local density of twin domains within a small particle size thereby renders $\Delta U_{SE}^{M\rightarrow T}$ strongly negative and further contributes to the depression of the transition temperature. Defects and dimensional confinement thus provide additional degrees of freedom beyond dopant incorporation and strain/pressure to access metastable polymorphs.

7. CONCLUSIONS AND OUTLOOK

In this Feature Article, we have sought to highlight several aspects of a richly diverse emerging area of the chemical sciences, periodic solids away from equilibrium. A fundamental thesis underpinning the exploration of metastability is that composition does not result in structural destiny—that structure can be controlled independently from composition. Metastable phase space thus holds opportunities for unprecedented tuning of properties and functionality based on the exploration of multiple structural variations for the same composition. Improved understanding of metastability will enable a fundamental re-evaluation of canonical chemical concepts such as allowed and preferred oxidation states, coordination geometries, and the nature of chemical bonding, many of which are thus far informed greatly by equilibrium ideas.

Several of the governing principles and synthetic strategies underpinning stabilization of metastable compounds have been outlined, emphasizing the need to traverse energy landscapes with synthetic methods that can carefully deposit materials within local minima or transformation pathways that take materials across specific trajectories. Dopants, defects, interfaces, dimensional confinement, and strain/pressure can modify the landscapes and trajectories and thus facilitate stabilization of metastable polymorphs. Topochemical modification, dimensional confinement (typically to sub-10 nm dimensions), pressure (mechanical or chemical), and templated methods can provide access to wide range of metastable polymorphs with an abiding guiding principle being the stabilization of a compound under a constraint (temperature, pressure, chemical potential), where it represents the most energetically stable species, followed by the removal of the constraint to "trap" the material under ambient conditions.[34] What is urgently required is a clear framework for the predictive design, synthesis, and evaluation of the properties of metastable compounds. Such a framework requires addressing issues spanning the range from predictive design rules for identifying viable metastable polymorphs to a toolset of synthetic methods for preparing such structures, a clear understanding of the relative positioning of polymorphs along energy landscapes, and a fundamental understanding of chemical bonding and structural motifs that result in excursions away from the thermodynamic minimum. The stabilization of an expanded palette of HfO_2 and V_2O_5 polymorphs provides illustrative examples of both synthetic strategies as well as mechanistic elucidation of transformations and unprecedented functionality.[49,54,73,74] Novel metastable polymorphs have enabled unprecedented function inaccessible within thermodynamic minima such as promising reversible intercalation of Mg-ions (ζ-V_2O_5),[73] combination of a high dielectric constant and a large band gap (tetragonal HfO_2), and unprecedented ferroelectric behavior (orthorhombic HfO_2).

The close integration of theory and experiment is imperative to transcend longstanding chemical bottlenecks in the prediction, rationalization, and realization of new chemical compounds outside of global thermodynamic minima. Efficient computational mapping of energy landscapes requires the development of reliable sampling and interpolation methods and further must be benchmarked to experimental observations of changes in the atomistic and geometric structure underpinning transformations between polymorphs. The spatial and temporal resolution to study such phase transformations is now accessible based on

DOI: 10.1021/acs.jpcc.8b04622
J. Phys. Chem. C XXXX, XXX, XXX−XXX

methods such as HAADF STEM imaging, dynamical TEM imaging, ultrafast XUV measurements of phonon dynamics, and ultrafast X-ray absorption spectroscopy measurements. The predictive design of metastable structures will further provide new opportunities for emergent function in areas such as catalysis and energy storage that most often require function under conditions far from equilibrium.

■ ASSOCIATED CONTENT

Web-Enhanced Feature

Video 1, which depicts the sequence of atomic displacements that bring about the phase transformations in HfO_2, in AVI format is available in the online version of the paper.

■ AUTHOR INFORMATION

Corresponding Author

*E-mail: banerjee@chem.tamu.edu.

ORCID

Sarbajit Banerjee: 0000-0002-2028-4675

Author Contributions

The manuscript was written through contributions of all authors. All authors have given approval to the final version of the manuscript.

Notes

The authors declare no competing financial interest.

Biographies

Photo provided by Sheetal Digari

Abhishek Parija obtained his undergraduate degree from the Indian Institute of Technology Bombay and is currently a Ph.D. candidate at Texas A&M University, where his research is focused on the computational design, synthesis, and spectroscopic identification of intercalation hosts and electrocatalysts. He is furthermore an Advanced Light Source—Molecular Foundry Doctoral Fellow at Lawrence Berkeley National Laboratory.

Gregory R. Waetzig earned an undergraduate degree from the University of Wyoming in 2013 and a Ph.D. in inorganic chemistry from Texas A&M University in 2018, where he was supervised by Prof. Sarbajit Banerjee. His doctoral research was focused on the design, synthesis, and functional applications of ceramic materials prepared with precise compositional, dimensional, and structural control from molecular precursors using the versatile nonhydrolytic sol−gel condensation process. He is currently a PTD Module & Integration Yield Engineer at Intel Corporation.

Photo provided by Karen D. Andrews

Justin L. Andrews obtained his undergraduate degree from Gordon College in Wenham, MA and is currently a Ph.D. candidate and NASA Space Technology Research Fellow at Texas A&M University. His research focuses on the design, stabilization, and evaluation of metastable materials for electrochemical energy storage and neuromorphic computing.

Photo provided by Chris Jarvis

Sarbajit Banerjee is the Davidson Professor of Science at Texas A&M University. He was a postdoctoral research scientist at the Department of Applied Physics and Applied Mathematics at Columbia University prior to starting his independent career at the State University of New York at Buffalo in 2007, where he served as the Co-Director of the New York State Center of Excellence in Materials Informatics. At SUNY-Buffalo, he was promoted to the rank of Associate Professor in 2012. In 2014, Prof. Banerjee moved to Texas A&M University as a Professor of Chemistry and Materials Science and Engineering. His research interests are focused on electron-correlated solids, methods for elucidating electronic structure, metastable materials, heterogeneous catalysis, and energy conversion and storage. He is a Fellow of the Royal Society of Chemistry and the Institute of Physics. Further information is available at http://www.chem.tamu.edu/rgroup/banerjee/.

DOI: 10.1021/acs.jpcc.8b04622
J. Phys. Chem. C XXXX, XXX, XXX−XXX

■ ACKNOWLEDGMENTS

We gratefully acknowledge our following collaborators for their insight, encouragement, and inspiration: Beth Guiton (University of Kentucky), Raymundo Arroyave (Texas A&M University), David Prendergast (LBNL), Louis F. J. Piper (Binghamton University), Peihong Zhang (University at Buffalo), and Alexander Moewes (University of Saskatchewan). This study is based on work supported by the National Science Foundation (NSF) under DMR 1809866. A.P. acknowledges support from the Advanced Light Source (ALS) doctoral fellowship in residence. The Advanced Light Source is supported by the Director, Office of Science, Office of Basic Energy Sciences of the U.S. Department of Energy under contract no. DE-AC02-05CH11231. A portion of the calculations were executed at the Molecular Foundry, Lawrence Berkeley National Laboratory, which is supported by the Office of Science, Office of Basic Energy Sciences of the U.S. Department of Energy under contract number DE-AC02-05CH11231. We acknowledge the Texas A&M Supercomputing Facility for computational resources. J.L.A. acknowledges support from a NASA Fellowship under 80NSSC17K0182.

■ REFERENCES

(1) Woodley, S. M.; Catlow, R. Crystal Structure Prediction from First Principles. *Nat. Mater.* 2008, *7*, 937.

(2) Wang, Y.; Lv, J.; Zhu, L.; Ma, Y. Crystal Structure Prediction via Particle-Swarm Optimization. *Phys. Rev. B: Condens. Matter Mater. Phys.* 2010, *82*, 094116.

(3) Oganov, A. R.; Lyakhov, A. O.; Valle, M. How Evolutionary Crystal Structure Prediction Works and Why. *Acc. Chem. Res.* 2011, *44*, 227−237.

(4) Navrotsky, A. Nanoscale Effects on Thermodynamics and Phase Equilibria in Oxide Systems. *ChemPhysChem* 2011, *12*, 2207−2215.

(5) Marley, P. M.; Horrocks, G. A.; Pelcher, K. E.; Banerjee, S. Transformers: The Changing Phases of Low-Dimensional Vanadium Oxide Bronzes. *Chem. Commun.* 2015, *51*, 5181−5198.

(6) Whittaker, L.; Patridge, C. J.; Banerjee, S. Microscopic and Nanoscale Perspective of the Metal−Insulator Phase Transitions of VO_2: Some New Twists to an Old Tale. *J. Phys. Chem. Lett.* 2011, *2*, 745−758.

(7) Navrotsky, A.; Mazeina, L.; Majzlan, J. Size-Driven Structural and Thermodynamic Complexity in Iron Oxides. *Science* 2008, *319*, 1635−1638.

(8) Waitz, T.; Tsuchiya, K.; Antretter, T.; Fischer, F. Phase Transformations of Nanocrystalline Martensitic Materials. *MRS Bull.* 2009, *34*, 814−821.

(9) Oganov, A. R.; Glass, C. W. Crystal Structure Prediction using ab initio Evolutionary Techniques: Principles and Applications. *J. Chem. Phys.* 2006, *124*, 244704.

(10) Turnbull, D. Metastable Structures in Metallurgy. *Metall. Trans. A* 1981, *12*, 695−708.

(11) Angus, J. C.; Hayman, C. C. Low-pressure, Metastable Growth of Diamond and "Diamondlike" Phases. *Science* 1988, *241*, 913−921.

(12) Angus, J. C.; Wang, Y.; Sunkara, M. Metastable Growth of Diamond and Diamond-like phases. *Annu. Rev. Mater. Sci.* 1991, *21*, 221−248.

(13) Lukowski, M. A.; Daniel, A. S.; Meng, F.; Forticaux, A.; Li, L.; Jin, S. Enhanced Hydrogen Evolution Catalysis from Chemically Exfoliated Metallic MoS_2 Nanosheets. *J. Am. Chem. Soc.* 2013, *135*, 10274−10277.

(14) Voiry, D.; Salehi, M.; Silva, R.; Fujita, T.; Chen, M.; Asefa, T.; Shenoy, V. B.; Eda, G.; Chhowalla, M. Conducting MoS_2 Nanosheets as Catalysts for Hydrogen Evolution Reaction. *Nano Lett.* 2013, *13*, 6222−6227.

(15) Nasr Esfahani, D.; Leenaerts, O.; Sahin, H.; Partoens, B.; Peeters, F. M. Structural Transitions in Monolayer MoS_2 by Lithium Adsorption. *J. Phys. Chem. C* 2015, *119*, 10602−10609.

(16) Liu, H.; Strobridge, F. C.; Borkiewicz, O. J.; Wiaderek, K. M.; Chapman, K. W.; Chupas, P. J.; Grey, C. P. Capturing Metastable Structures During High-Rate Cycling of $LiFePO_4$ Nanoparticle Electrodes. *Science* 2014, *344*, 1252817.

(17) Zhao, Y.; De Jesus, L. R.; Stein, P.; Horrocks, G. A.; Banerjee, S.; Xu, B.-X. Modeling of Phase Separation across Interconnected Electrode Particles in Lithium-Ion Batteries. *RSC Adv.* 2017, *7*, 41254−41264.

(18) Somani, M.; Juntunen, P.; Karjalainen, L.; Misra, R.; Kyröläinen, A. Enhanced Mechanical Properties through Reversion in Metastable Austenitic Stainless Steels. *Metall. Mater. Trans. A* 2009, *40*, 729−744.

(19) Datta, K.; Delhez, R.; Bronsveld, P.; Beyer, J.; Geijselaers, H. J.; Post, J. A Low-Temperature Study to Examine the Role of ε-Martensite During Strain-Induced Transformations in Metastable Austenitic Stainless Steels. *Acta Mater.* 2009, *57*, 3321−3326.

(20) Gopalakrishnan, J. Chimie Douce Approaches to the Synthesis of Metastable Oxide Materials. *Chem. Mater.* 1995, *7*, 1265−1275.

(21) Stein, A.; Keller, S. W.; Mallouk, T. E. Turning Down the Heat: Design and Mechanism in Solid-State Synthesis. *Science* 1993, *259*, 1558−1564.

(22) Jansen, M. A Concept for Synthesis Planning in Solid-State Chemistry. *Angew. Chem., Int. Ed.* 2002, *41*, 3746−3766.

(23) Price, S. L. Why Don't We Find More Polymorphs? *Acta Crystallogr., Sect. B: Struct. Sci., Cryst. Eng. Mater.* 2013, *69*, 313−328.

(24) Stevanović, V.; Trottier, R.; Musgrave, C.; Therrien, F.; Holder, A.; Graf, P. Predicting Kinetics of Polymorphic Transformations from Structure Mapping and Coordination Analysis. *Phys. Rev. Mater.* 2018, *2*, 033802.

(25) Lonie, D. C.; Zurek, E. XtalOpt: An Open-Source Evolutionary Algorithm for Crystal Structure Prediction. *Comput. Phys. Commun.* 2011, *182*, 372−387.

(26) Shamp, A.; Terpstra, T.; Bi, T.; Falls, Z.; Avery, P.; Zurek, E. Decomposition Products of Phosphine under Pressure: PH_2 Stable and Superconducting? *J. Am. Chem. Soc.* 2016, *138*, 1884−1892.

(27) Zurek, E.; Yao, Y. Theoretical Predictions of Novel Superconducting Phases of $BaGe_3$ Stable at Atmospheric and High Pressures. *Inorg. Chem.* 2015, *54*, 2875−2884.

(28) Castillo, R.; Baranov, A. I.; Burkhardt, U.; Cardoso-Gil, R.; Schnelle, W.; Bobnar, M.; Schwarz, U. Germanium Dumbbells in a New Superconducting Modification of $BaGe_3$. *Inorg. Chem.* 2016, *55*, 4498−4503.

(29) Stevanović, V. Sampling Polymorphs of Ionic Solids using Random Superlattices. *Phys. Rev. Lett.* 2016, *116*, 075503.

(30) Curtarolo, S.; Hart, G. L.; Nardelli, M. B.; Mingo, N.; Sanvito, S.; Levy, O. The High-Throughput Highway to Computational Materials Design. *Nat. Mater.* 2013, *12*, 191.

(31) Jain, A.; Ong, S. P.; Hautier, G.; Chen, W.; Richards, W. D.; Dacek, S.; Cholia, S.; Gunter, D.; Skinner, D.; Ceder, G.; et al. Commentary: The Materials Project: A Materials Genome Approach to Accelerating Materials Innovation. *APL Mater.* 2013, *1*, 011002.

(32) Saal, J. E.; Kirklin, S.; Aykol, M.; Meredig, B.; Wolverton, C. Materials Design and Discovery with High-Throughput Density Functional Theory: The Open Quantum Materials Database (OQMD). *JOM* 2013, *65*, 1501−1509.

(33) Curtarolo, S.; Setyawan, W.; Wang, S.; Xue, J.; Yang, K.; Taylor, R. H.; Nelson, L. J.; Hart, G. L.; Sanvito, S.; Buongiorno-Nardelli, M.; et al. AFLOWLIB. ORG: A Distributed Materials Properties Repository from High-Throughput ab initio Calculations. *Comput. Mater. Sci.* 2012, *58*, 227−235.

(34) Sun, W.; Dacek, S. T.; Ong, S. P.; Hautier, G.; Jain, A.; Richards, W. D.; Gamst, A. C.; Persson, K. A.; Ceder, G. The Thermodynamic Scale of Inorganic Crystalline Metastability. *Sci. Adv.* 2016, *2*, e1600225.

(35) Reed, J.; Ceder, G. Role of Electronic Structure in the Susceptibility of Metastable Transition-Metal Oxide Structures to Transformation. *Chem. Rev.* 2004, *104*, 4513−4534.

(36) O'Hara, A.; Demkov, A. A. Nature of the Metal-Insulator Transition in NbO_2. *Phys. Rev. B: Condens. Matter Mater. Phys.* 2015, *91*, 094305.

DOI: 10.1021/acs.jpcc.8b04622
J. Phys. Chem. C XXXX, XXX, XXX−XXX

(37) Brito, W.; Aguiar, M.; Haule, K.; Kotliar, G. Dynamic Electronic Correlation Effects in NbO_2 as Compared to VO_2. *Phys. Rev. B: Condens. Matter Mater. Phys.* 2017, *96*, 195102.

(38) Caspersen, K. J.; Carter, E. A. Finding Transition States for Crystalline Solid−Solid Phase Transformations. *Proc. Natl. Acad. Sci. U. S. A.* 2005, *102*, 6738−6743.

(39) Sheppard, D.; Xiao, P.; Chemelewski, W.; Johnson, D. D.; Henkelman, G. A Generalized Solid-State Nudged Elastic Band Method. *J. Chem. Phys.* 2012, *136*, 074103.

(40) Qian, G.-R.; Dong, X.; Zhou, X.-F.; Tian, Y.; Oganov, A. R.; Wang, H.-T. Variable Cell Nudged Elastic Band Method for Studying Solid−Solid Structural Phase Transitions. *Comput. Phys. Commun.* 2013, *184*, 2111−2118.

(41) Bajaj, S.; Haverty, M. G.; Arróyave, R.; Goddard, W. A., III; Shankar, S. Phase Stability in Nanoscale Material Systems: Extension From Bulk Phase Diagrams. *Nanoscale* 2015, *7*, 9868−9877.

(42) Powell, A. E.; Hodges, J. M.; Schaak, R. E. Preserving Both Anion and Cation Sublattice Features during a Nanocrystal Cation-Exchange Reaction: Synthesis of Metastable Wurtzite-Type CoS and MnS. *J. Am. Chem. Soc.* 2016, *138*, 471−474.

(43) Saha, D.; Jensen, K. M.; Tyrsted, C.; Bøjesen, E. D.; Mamakhel, A. H.; Dippel, A. C.; Christensen, M.; Iversen, B. B. In Situ Total X-Ray Scattering Study of WO_3 Nanoparticle Formation under Hydrothermal Conditions. *Angew. Chem., Int. Ed.* 2014, *53*, 3667−3670.

(44) Nayak, A. P.; Bhattacharyya, S.; Zhu, J.; Liu, J.; Wu, X.; Pandey, T.; Jin, C.; Singh, A. K.; Akinwande, D.; Lin, J.-F. Pressure-Induced Semiconducting to Metallic Transition in Multilayered Molybdenum Disulphide. *Nat. Commun.* 2014, *5*, 3731.

(45) Seddon, J.; Suard, E.; Hayward, M. A. Topotactic Reduction of $YBaCo_2O_5$ and $LaBaCo_2O_5$: Square-Planar Co (I) in an Extended Oxide. *J. Am. Chem. Soc.* 2010, *132*, 2802−2810.

(46) Schaak, R. E.; Mallouk, T. E. Topochemical Synthesis of Three-Dimensional Perovskites from Lamellar Precursors. *J. Am. Chem. Soc.* 2000, *122*, 2798−2803.

(47) Bianco, E.; Butler, S.; Jiang, S.; Restrepo, O. D.; Windl, W.; Goldberger, J. E. Stability and Exfoliation of Germanane: A Germanium Graphane Analogue. *ACS Nano* 2013, *7*, 4414−4421.

(48) Cultrara, N. D.; Wang, Y.; Arguilla, M. Q.; Scudder, M. R.; Jiang, S.; Windl, W.; Bobev, S.; Goldberger, J. E. Synthesis of 1T, 2H, and 6R Germanane Polytypes. *Chem. Mater.* 2018, *30*, 1335−1343.

(49) Waetzig, G. R.; Horrocks, G. A.; Jude, J. W.; Zuin, L.; Banerjee, S. X-ray Excited Photoluminescence near the Giant Resonance in Solid-Solution $Gd_{1-x}Tb_xOCl$ Nanocrystals and their Retention upon Solvothermal Topotactic Transformation to $Gd_{1-x}Tb_xF_3$. *Nanoscale* 2016, *8*, 979−986.

(50) Ranade, M.; Navrotsky, A.; Zhang, H.; Banfield, J.; Elder, S.; Zaban, A.; Borse, P.; Kulkarni, S.; Doran, G.; Whitfield, H. Energetics of Nanocrystalline TiO_2. *Proc. Natl. Acad. Sci. U. S. A.* 2002, *99*, 6476−6481.

(51) Garvie, R. C. The Occurrence of Metastable Tetragonal Zirconia as a Crystallite Size Effect. *J. Phys. Chem.* 1965, *69*, 1238−1243.

(52) Garvie, R. Stabilization of the Tetragonal Structure in Zirconia Microcrystals. *J. Phys. Chem.* 1978, *82*, 218−224.

(53) Waetzig, G. R.; Depner, S. W.; Asayesh-Ardakani, H.; Cultrara, N. D.; Shahbazian-Yassar, R.; Banerjee, S. Stabilizing Metastable Tetragonal HfO_2 using a Non-Hydrolytic Solution-Phase Route: Ligand Exchange as a Means of Controlling Particle Size. *Chem. Sci.* 2016, *7*, 4930−4939.

(54) Hudak, B. M.; Depner, S. W.; Waetzig, G. R.; Talapatra, A.; Arroyave, R.; Banerjee, S.; Guiton, B. S. Real-Time Atomistic Observation of Structural Phase Transformations in Individual Hafnia Nanorods. *Nat. Commun.* 2017, *8*, 15316.

(55) Farrow, R. The Stabilization of Metastable Phases by Epitaxy. *J. Vac. Sci. Technol., B: Microelectron. Process. Phenom.* 1983, *1*, 222−228.

(56) David, L.; Bradford, C.; Tang, X.; Graham, T.; Prior, K.; Cavenett, B. Growth of Zinc Blende MnS and MnS Heterostructures by MBE using ZnS as a Sulfur Source. *J. Cryst. Growth* 2003, *251*, 591−595.

(57) Quackenbush, N.; Paik, H.; Wahila, M.; Sallis, S.; Holtz, M.; Huang, X.; Ganose, A.; Morgan, B.; Scanlon, D. O.; Gu, Y.; et al. Stability of the M2 Phase of Vanadium Dioxide Induced by Coherent Epitaxial Strain. *Phys. Rev. B: Condens. Matter Mater. Phys.* 2016, *94*, 085105.

(58) Park, J. H.; Coy, J. M.; Kasirga, T. S.; Huang, C.; Fei, Z.; Hunter, S.; Cobden, D. H. Measurement of a Solid-State Triple Point at the Metal−Insulator Transition in VO_2. *Nature* 2013, *500*, 431.

(59) Braham, E. J.; Sellers, D.; Emmons, E.; Villarreal, R.; Asayesh-Ardakani, H.; Fleer, N. A.; Farley, K. E.; Shahbazian-Yassar, R.; Arròyave, R.; Shamberger, P. J.; et al. Modulating the Hysteresis of an Electronic Transition: Launching Alternative Transformation Pathways in the Metal−Insulator Transition of Vanadium (IV) Oxide. *Chem. Mater.* 2018, *30*, 214−224.

(60) Asayesh-Ardakani, H.; Nie, A.; Marley, P. M.; Zhu, Y.; Phillips, P. J.; Singh, S.; Mashayek, F.; Sambandamurthy, G.; Low, K.-b.; Klie, R. F.; et al. Atomic Origins of Monoclinic-Tetragonal (Rutile) Phase Transition in Doped VO_2 Nanowires. *Nano Lett.* 2015, *15*, 7179−7188.

(61) Birgisson, S.; Saha, D.; Iversen, B. B. Formation Mechanisms of Nanocrystalline MnO_2 Polymorphs under Hydrothermal Conditions. *Cryst. Growth Des.* 2018, *18*, 827−838.

(62) Tuller, H. L.; Bishop, S. R. Point Defects in Oxides: Tailoring Materials Through Defect Engineering. *Annu. Rev. Mater. Res.* 2011, *41*, 369−398.

(63) Batra, R.; Huan, T. D.; Rossetti, G. A., Jr; Ramprasad, R. Dopants Promoting Ferroelectricity in Hafnia: Insights from a Comprehensive Chemical Space Exploration. *Chem. Mater.* 2017, *29*, 9102−9109.

(64) Huan, T. D.; Sharma, V.; Rossetti, G. A., Jr; Ramprasad, R. Pathways Towards Ferroelectricity in Hafnia. *Phys. Rev. B: Condens. Matter Mater. Phys.* 2014, *90*, 064111.

(65) Kappera, R.; Voiry, D.; Yalcin, S. E.; Branch, B.; Gupta, G.; Mohite, A. D.; Chhowalla, M. Phase-Engineered Low-Resistance Contacts for Ultrathin MoS_2 Transistors. *Nat. Mater.* 2014, *13*, 1128.

(66) Wang, Y.; Xiao, J.; Zhu, H.; Li, Y.; Alsaid, Y.; Fong, K. Y.; Zhou, Y.; Wang, S.; Shi, W.; Wang, Y.; et al. Structural Phase Transition in Monolayer $MoTe_2$ Driven by Electrostatic Doping. *Nature* 2017, *550*, 487.

(67) Filinchuk, Y.; Tumanov, N. A.; Ban, V.; Ji, H.; Wei, J.; Swift, M. W.; Nevidomskyy, A. H.; Natelson, D. In Situ Diffraction Study of Catalytic Hydrogenation of VO_2: Stable Phases and Origins of Metallicity. *J. Am. Chem. Soc.* 2014, *136*, 8100−8109.

(68) Alivio, T. E.; Sellers, D. G.; Asayesh-Ardakani, H.; Braham, E. J.; Horrocks, G. A.; Pelcher, K. E.; Villareal, R.; Zuin, L.; Shamberger, P. J.; Arroyave, R.; et al. Postsynthetic Route for Modifying the Metal-Insulator Transition of VO_2 by Interstitial Dopant Incorporation. *Chem. Mater.* 2017, *29*, 5401−5412.

(69) Flores-Livas, J. A.; Sanna, A.; Drozdov, A. P.; Boeri, L.; Profeta, G.; Eremets, M.; Goedecker, S. Interplay Between Structure and Superconductivity: Metastable Phases of Phosphorus under Pressure. *Phys. Rev. Mater.* 2017, *1*, 024802.

(70) Filonenko, V.; Sundberg, M.; Werner, P.-E.; Zibrov, I. Structure of a High-Pressure Phase of Vanadium Pentoxide, β-V_2O_5. *Acta Crystallogr., Sect. B: Struct. Sci.* 2004, *60*, 375−381.

(71) Tolhurst, T. M.; Leedahl, B.; Andrews, J. L.; Marley, P. M.; Banerjee, S.; Moewes, A. Contrasting 1D Tunnel-Structured and 2D Layered Polymorphs of V_2O_5: Relating Crystal Structure and Bonding to Band Gaps and Electronic Structure. *Phys. Chem. Chem. Phys.* 2016, *18*, 15798−15806.

(72) De Jesus, L. R.; Andrews, J. L.; Parija, A.; Banerjee, S. Defining Diffusion Pathways in Intercalation Cathode Materials: Some Lessons from V_2O_5 on Directing Cation Traffic. *ACS Energy Lett.* 2018, *3*, 915−931.

(73) Andrews, J. L.; Mukherjee, A.; Yoo, H. D.; Parija, A.; Marley, P. M.; Fakra, S.; Prendergast, D.; Cabana, J.; Klie, R. F.; Banerjee, S. Reversible Mg-Ion Insertion in a Metastable One-Dimensional Polymorph of V_2O_5. *Chem.* 2018, *4*, 564−585.

(74) Parija, A.; Liang, Y.; Andrews, J. L.; De Jesus, L. R.; Prendergast, D.; Banerjee, S. Topochemically De-Intercalated Phases of V_2O_5 as

Cathode Materials for Multivalent Intercalation Batteries: A First-Principles Evaluation. *Chem. Mater.* **2016**, *28*, 5611−5620.

(75) Parija, A.; Prendergast, D.; Banerjee, S. Evaluation of Multivalent Cation Insertion in Single-and Double-Layered Polymorphs of V_2O_5. *ACS Appl. Mater. Interfaces* **2017**, *9*, 23756−23765.

(76) Gutowski, M.; Jaffe, J. E.; Liu, C.-L.; Stoker, M.; Hegde, R. I.; Rai, R. S.; Tobin, P. J. Thermodynamic Stability of High-K Dielectric Metal Oxides ZrO_2 and HfO_2 in Contact with Si and SiO_2. *Appl. Phys. Lett.* **2002**, *80*, 1897−1899.

(77) Jiang, H.; Gomez-Abal, R. I.; Rinke, P.; Scheffler, M. Electronic Band Structure of Zirconia and Hafnia Polymorphs from the GW Perspective. *Phys. Rev. B: Condens. Matter Mater. Phys.* **2010**, *81*, 085119.

(78) Zhao, X.; Vanderbilt, D. First-Principles Study of Structural, Vibrational, and Lattice Dielectric Properties of Hafnium Oxide. *Phys. Rev. B: Condens. Matter Mater. Phys.* **2002**, *65*, 233106.

(79) Tarascon, J.; Vaughan, G.; Chabre, Y.; Seguin, L.; Anne, M.; Strobel, P.; Amatucci, G. In Situ Structural and Electrochemical Study of $Ni_{1-x}Co_xO_2$ Metastable Oxides Prepared by Soft Chemistry. *J. Solid State Chem.* **1999**, *147*, 410−420.

(80) Orikasa, Y.; Maeda, T.; Koyama, Y.; Murayama, H.; Fukuda, K.; Tanida, H.; Arai, H.; Matsubara, E.; Uchimoto, Y.; Ogumi, Z. Direct Observation of a Metastable Crystal Phase of Li_xFePO_4 under Electrochemical Phase Transition. *J. Am. Chem. Soc.* **2013**, *135*, 5497−5500.

(81) Liu, C.; Neale, Z. G.; Cao, G. Understanding Electrochemical Potentials of Cathode Materials in Rechargeable Batteries. *Mater. Today* **2016**, *19*, 109−123.

(82) Goodenough, J. B.; Kim, Y. Challenges for Rechargeable Li Batteries. *Chem. Mater.* **2010**, *22*, 587−603.

(83) Wang, J.; Chen-Wiegart, Y.-c. K.; Wang, J. In Operando Tracking Phase Transformation Evolution of Lithium Iron Phosphate with Hard X-ray Microscopy. *Nat. Commun.* **2014**, *5*, 4570.

(84) Love, C. T.; Korovina, A.; Patridge, C. J.; Swider-Lyons, K. E.; Twigg, M. E.; Ramaker, D. E. Review of $LiFePO_4$ Phase Transition Mechanisms and New Observations From X-Ray Absorption Spectroscopy. *J. Electrochem. Soc.* **2013**, *160*, A3153−A3161.

(85) Zhao, J.; Tao, Z.; Liang, J.; Chen, J. Facile Synthesis of Nanoporous γ-MnO_2 Structures and their Application in Rechargeable Li-ion Batteries. *Cryst. Growth Des.* **2008**, *8*, 2799−2805.

(86) Greedan, J. E.; Raju, N.; Wills, A.; Morin, C.; Shaw, S.; Reimers, J. Structure and Magnetism in λ-MnO_2. Geometric Frustration in a Defect Spinel. *Chem. Mater.* **1998**, *10*, 3058−3067.

(87) Capitaine, F.; Gravereau, P.; Delmas, C. A New Variety of $LiMnO_2$ with a Layered Structure. *Solid State Ionics* **1996**, *89*, 197−202.

(88) Kitchaev, D. A.; Peng, H.; Liu, Y.; Sun, J.; Perdew, J. P.; Ceder, G. Energetics of MnO_2 Polymorphs in Density Functional Theory. *Phys. Rev. B: Condens. Matter Mater. Phys.* **2016**, *93*, 045132.

(89) Han, S.-D.; Kim, S.; Li, D.; Petkov, V.; Yoo, H. D.; Phillips, P. J.; Wang, H.; Kim, J. J.; More, K. L.; Key, B.; et al. Mechanism of Zn Insertion into Nanostructured δ-MnO_2: A Nonaqueous Rechargeable Zn Metal Battery. *Chem. Mater.* **2017**, *29*, 4874−4884.

(90) Lipson, A. L.; Pan, B.; Lapidus, S. H.; Liao, C.; Vaughey, J. T.; Ingram, B. J. Rechargeable Ca-ion Batteries: A New Energy Storage System. *Chem. Mater.* **2015**, *27*, 8442−8447.

(91) Zavalij, P. Y.; Whittingham, M. S. Structural Chemistry of Vanadium Oxides with Open Frameworks. *Acta Crystallogr., Sect. B: Struct. Sci.* **1999**, *55*, 627−663.

(92) Horrocks, G. A.; Parija, A.; De Jesus, L. R.; Wangoh, L.; Sallis, S.; Luo, Y.; Andrews, J. L.; Jude, J.; Jaye, C.; Fischer, D. A.; et al. Mitigating Cation Diffusion Limitations and Intercalation-Induced Framework Transitions in a 1D Tunnel-Structured Polymorph of V_2O_5. *Chem. Mater.* **2017**, *29*, 10386−10397.

(93) Pouchard, M.; Hagenmuller, P. The System $K_xV_2O_5$ of a Few Novel Families of Vanadium Oxibronzes. *Mater. Res. Bull.* **1967**, *2*, 799−808.

(94) Savariault, J.-M.; Parize, J.-L.; Ballivet-Tkatchendo, D.; Galy, J. τ-$Na_xV_2O_5$ (x= 0.64): A Vanadium Bronze with an Original Intergrowth Structure. *J. Solid State Chem.* **1996**, *122*, 1−6.

(95) Waltersson, K.; Forslund, B. A Refinement of the Crystal Structure of CsV_2O_5. *Acta Crystallogr., Sect. B: Struct. Crystallogr. Cryst. Chem.* **1977**, *33*, 789−793.

(96) Waltersson, K.; Forslund, B. On the Crystal Structure of $Cs_xV_3O_7$ ($x \sim 0.35$), A New Hexagonal Vanadium Bronze Structure Type. *Acta Crystallogr., Sect. B: Struct. Crystallogr. Cryst. Chem.* **1977**, *33*, 775−779.

(97) Oka, Y.; Tamada, O.; Yao, T.; Yamamoto, N. Hydrothermal Synthesis and Crystal Structure of a Novel Barium Vanadium Oxide: $Ba_{0.4}V_3O_8(VO)_{0.4}\cdot nH_2O$. *J. Solid State Chem.* **1995**, *114*, 359−363.

(98) Yamauchi, T.; Ueda, H.; Ueda, Y.; Kikuchi, J. Rich Phase Transitions Under Pressure in β-$A_{0.33}V_2O_5$ (A= Ca and Pb). *Phys. C* **2007**, *460*, 532−533.

(99) Marley, P. M.; Singh, S.; Abtew, T. A.; Jaye, C.; Fischer, D. A.; Zhang, P.; Sambandamurthy, G.; Banerjee, S. Electronic Phase Transitions of δ-$Ag_xV_2O_5$ Nanowires: Interplay Between Geometric and Electronic Structures. *J. Phys. Chem. C* **2014**, *118*, 21235−21243.

(100) Patridge, C. J.; Wu, T.-L.; Sambandamurthy, G.; Banerjee, S. Colossal Above-Room-Temperature Metal−Insulator Switching of a Wadsley-Type Tunnel Bronze. *Chem. Commun.* **2011**, *47*, 4484−4486.

(101) Permer, L.; Ferey, G. Crystal Structure of β'-$Fe_{0.33}V_2O_5$. *Z. Kristallogr.* **1994**, *209*, 413−417.

(102) Chirayil, T. Z.; Zavalij, P. Y.; Whittingham, M. S. Synthesis and Characterization of a New Vanadium Oxide, $TMAV_8O_{20}$. *J. Mater. Chem.* **1997**, *7*, 2193−2195.

(103) Zhang, Y. H.; Haushalter, R. C.; Clearfield, A. Hydrothermal Syntheses and Structural Characterization of Layered Vanadium Oxides Incorporating Organic Cations: α-, β- $(H_3N(CH_2)_2NH_3)$-$[V_4O_{10}]$ and α-, β-$(H_2N(C_2H_4)_2NH_2)[V_4O_{10}]$. *Inorg. Chem.* **1996**, *35*, 4950−4956.

(104) Horrocks, G. A.; Likely, M. F.; Velazquez, J. M.; Banerjee, S. Finite Size Effects on the Structural Progression Induced by Lithiation of V_2O_5: A Combined Diffraction and Raman Spectroscopy Study. *J. Mater. Chem. A* **2013**, *1*, 15265−15277.

(105) Cocciantelli, J.; Gravereau, P.; Doumerc, J.; Pouchard, M.; Hagenmuller, P. On the Preparation and Characterization of a New Polymorph of V_2O_5. *J. Solid State Chem.* **1991**, *93*, 497−502.

(106) Zibrov, I. P.; Filonenko, V. P.; Lyapin, S. G.; Sidorov, V. A. The High Pressure Phases β-and δ-V_2O_5: Structure Refinement, Electrical and Optical Properties, Thermal Stability. *High Pressure Res.* **2013**, *33*, 399−408.

(107) Marley, P. M.; Abtew, T. A.; Farley, K. E.; Horrocks, G. A.; Dennis, R. V.; Zhang, P.; Banerjee, S. Emptying and Filling a Tunnel Bronze. *Chem. Sci.* **2015**, *6*, 1712−1718.

(108) De Jesus, L. R.; Horrocks, G. A.; Liang, Y.; Parija, A.; Jaye, C.; Wangoh, L.; Wang, J.; Fischer, D. A.; Piper, L. F.; Prendergast, D.; et al. Mapping Polaronic States and Lithiation Gradients in Individual V_2O_5 Nanowires. *Nat. Commun.* **2016**, *7*, 12022.

(109) Enjalbert, R.; Galy, J. A Refinement of the Structure of V_2O_5. *Acta Crystallogr., Sect. C: Cryst. Struct. Commun.* **1986**, *42*, 1467−1469.

(110) Galy, J. Vanadium Pentoxide and Vanadium Oxide Bronzes—Structural Chemistry of Single (S) and Double (D) Layer $M_xV_2O_5$ Phases. *J. Solid State Chem.* **1992**, *100*, 229−245.

(111) Bystrom, A.; Wilhelmi, K.; Brotzen, O. Vanadium Pentoxide-A Compound with Five-Coordinated Vanadium Atoms. *Acta Chem. Scand.* **1950**, *4*, 1119.

(112) Satto, C.; Sciau, P.; Dooryhee, E.; Galy, J.; Millet, P. The $\delta \rightarrow \varepsilon \rightarrow \gamma$ LiV_2O_5 "High Temperature" Phase Transitions Evidenced by Synchrotron X-Ray Powder Diffraction Analysis. *J. Solid State Chem.* **1999**, *146*, 103−109.

(113) Marley, P. M.; Banerjee, S. Reversible Interconversion of a Divalent Vanadium Bronze between δ and β Quasi-1D Structures. *Inorg. Chem.* **2012**, *51*, 5264−5269.

(114) Delmas, C.; Cognac-Auradou, H.; Cocciantelli, J.; Menetrier, M.; Doumerc, J. The $Li_xV_2O_5$ System: An Overview of the Structure Modifications Induced by the Lithium Intercalation. *Solid State Ionics* **1994**, *69*, 257−264.

(115) Gershinsky, G.; Yoo, H. D.; Gofer, Y.; Aurbach, D. Electrochemical and Spectroscopic Analysis of Mg^{2+} Intercalation

Into thin Film Electrodes of Layered Oxides: V_2O_5 and MoO_3. *Langmuir* 2013, *29*, 10964−10972.

(116) Rong, Z.; Malik, R.; Canepa, P.; Sai Gautam, G.; Liu, M.; Jain, A.; Persson, K.; Ceder, G. Materials Design Rules for Multivalent Ion Mobility in Intercalation Structures. *Chem. Mater.* 2015, *27*, 6016−6021.

(117) Gautam, G. S.; Canepa, P.; Malik, R.; Liu, M.; Persson, K.; Ceder, G. First-Principles Evaluation of Multi-Valent Cation Insertion Into Orthorhombic V_2O_5. *Chem. Commun.* 2015, *51*, 13619−13622.

(118) Sanchez, C.; Henry, M.; Morineau, R.; Leroy, M. Small Polaron Mobility in α-Li_xO_5. *Phys. Status Solidi B* 1984, *122*, 175−182.

(119) Maxisch, T.; Zhou, F.; Ceder, G. Ab initio Study of the Migration of Small Polarons in Olivine Li_xFePO_4 and their Association with Lithium Ions and Vacancies. *Phys. Rev. B: Condens. Matter Mater. Phys.* 2006, *73*, 104301.

(120) De Jesus, L. R.; Stein, P.; Andrews, J. L.; Luo, Y.; Xu, B.-X.; Banerjee, S. Striping Modulations and Strain Gradients within Individual Particles of a Cathode Material Upon Lithiation. *Mater. Horiz.* 2018, *5*, 486−498.

(121) Maganas, D.; Roemelt, M.; Hävecker, M.; Trunschke, A.; Knop-Gericke, A.; Schlögl, R.; Neese, F. First-Principles Calculations of the Structure and V L-edge X-ray Absorption Spectra of V_2O_5 using Local Pair Natural Orbital Coupled Cluster Theory and Spin−Orbit Coupled Configuration Interaction Approaches. *Phys. Chem. Chem. Phys.* 2013, *15*, 7260−7276.

(122) Velazquez, J. M.; Jaye, C.; Fischer, D. A.; Banerjee, S. Near Edge X-Ray Absorption Fine Structure Spectroscopy Studies of Single-Crystalline V_2O_5 Nanowire Arrays. *J. Phys. Chem. C* 2009, *113*, 7639−7645.

(123) Mukherjee, A.; Sa, N.; Phillips, P. J.; Burrell, A.; Vaughey, J.; Klie, R. F. Direct Investigation of Mg Intercalation Into the Orthorhombic V_2O_5 Cathode Using Atomic-Resolution Transmission Electron Microscopy. *Chem. Mater.* 2017, *29*, 2218−2226.

(124) Tolbert, S.; Alivisatos, A. Size Dependence of a First Order Solid-Solid Phase Transition: The Wurtzite to Rock Salt Transformation in CdSe Nanocrystals. *Science* 1994, *265*, 373−376.

(125) Grünwald, M.; Lutker, K.; Alivisatos, A. P.; Rabani, E.; Geissler, P. L. Metastability in Pressure-Induced Structural Transformations of CdSe/ZnS Core/Shell Nanocrystals. *Nano Lett.* 2013, *13*, 1367−1372.

(126) Batra, R.; Tran, H. D.; Ramprasad, R. Stabilization of Metastable Phases in Hafnia Owing to Surface Energy Effects. *Appl. Phys. Lett.* 2016, *108*, 172902.

(127) Luo, X.; Demkov, A. A. Structure, Thermodynamics, and Crystallization of Amorphous Hafnia. *J. Appl. Phys.* 2015, *118*, 124105.

(128) Tang, J.; Fabbri, J.; Robinson, R. D.; Zhu, Y.; Herman, I. P.; Steigerwald, M. L.; Brus, L. E. Solid-Solution Nanoparticles: Use of a Nonhydrolytic Sol− Gel Synthesis To Prepare HfO_2 and $Hf_xZr_{1-x}O_2$ Nanocrystals. *Chem. Mater.* 2004, *16*, 1336−1342.

(129) Clearfield, A. Structural Aspects of Zirconium Chemistry. *Rev. Pure Appl. Chem.* 1964, 14.

(130) Hf-O Binary Phase Diagram 0-80 at.% O: Datasheet from PAULING FILE Multinaries Edition, 2012. In *Inorganic Solid Phases, SpringerMaterials (online database)*; Villars, P., Okamoto, H., Eds.; Springer-Verlag Berlin Heidelberg & Material Phases Data System (MPDS), Switzerland & National Institute for Materials Science (NIMS), Japan, 2016.https://materials.springer.com/isp/phase-diagram/docs/c_0901278.

(131) Joo, J.; Yu, T.; Kim, Y. W.; Park, H. M.; Wu, F.; Zhang, J. Z.; Hyeon, T. Multigram Scale Synthesis and Characterization of Monodisperse Tetragonal Zirconia Nanocrystals. *J. Am. Chem. Soc.* 2003, *125*, 6553−6557.

(132) Shukla, S.; Seal, S. Mechanisms of Room Temperature Metastable Tetragonal Phase Stabilisation in Zirconia. *Int. Mater. Rev.* 2005, *50*, 45−64.

(133) Trolliard, G.; Mercurio, D.; Perez-Mato, J. M. Martensitic Phase Transition in Pure Zirconia: A Crystal Chemistry Viewpoint. *Z. Kristallogr. Cryst. Mater.* 2011, *226*, 264−290.

(134) Zhou, W.; Ushakov, S. V.; Wang, T.; Ekerdt, J. G.; Demkov, A. A.; Navrotsky, A. Hafnia: Energetics of Tthin Films and Nanoparticles. *J. Appl. Phys.* 2010, *107*, 123514.

(135) Depner, S. W.; Cultrara, N. D.; Farley, K. E.; Qin, Y.; Banerjee, S. Ferroelastic Domain Organization and Precursor Control of Size in Solution-Grown Hafnium Dioxide Nanorods. *ACS Nano* 2014, *8*, 4678−4688.

(136) Müller, J.; Böscke, T. S.; Schröder, U.; Mueller, S.; Bräuhaus, D.; Böttger, U.; Frey, L.; Mikolajick, T. Ferroelectricity in Simple Binary ZrO_2 and HfO_2. *Nano Lett.* 2012, *12*, 4318−4323.

(137) MacLaren, I.; Ras, T.; MacKenzie, M.; Craven, A.; McComb, D.; De Gendt, S. Texture, Twinning, and Metastable "Tetragonal" Phase in Ultrathin Films of HfO_2 on a Si Substrate. *J. Electrochem. Soc.* 2009, *156*, G103−G108.

(138) Boysen, H.; Frey, F.; Vogt, T. Neutron Powder Investigation of the Tetragonal to Monoclinic Phase Transformation in Undoped Zirconia. *Acta Crystallogr., Sect. B: Struct. Sci.* 1991, *47*, 881−886.

(139) Tang, J.; Zhang, F.; Zoogman, P.; Fabbri, J.; Chan, S. W.; Zhu, Y.; Brus, L. E.; Steigerwald, M. L. Martensitic Phase Transformation of Isolated HfO_2, ZrO_2, and $Hf_xZr_{1-x}O_2$ $(0 < x< 1)$ Nanocrystals. *Adv. Funct. Mater.* 2005, *15*, 1595−1602.

(140) Iskandarova, I.; Knizhnik, A.; Rykova, E.; Bagatur'yants, A.; Potapkin, B.; Korkin, A. First-Principle Investigation of the Hydroxylation of Zirconia and Hafnia Surfaces. *Microelectron. Eng.* 2003, *69*, 587−593.

(141) Wang, J.; Li, H.; Stevens, R. Hafnia and Hafnia-Toughened Ceramics. *J. Mater. Sci.* 1992, *27*, 5397−5430.

(142) Garvie, R.; Hannink, R.; Pascoe, R. Ceramic Steel? *Nature* 1975, *258*, 703.

(143) Nicoloso, N.; Löbert, A.; Leibold, B. Optical Absorption Studies of Tetragonal and Cubic Thin-Film Yttria-Stabilized Zirconia. *Sens. Actuators, B* 1992, *8*, 253−256.

(144) Virbukas, D.; Laukaitis, G.; Dudonis, J.; Milčius, D. The Properties of Scandium and Cerium Stabilized Zirconium Thin Films Formed by E-Beam Technique. *Solid State Ionics* 2011, *188*, 46−49.

(145) Zhou, B.; Shi, H.; Zhang, X.; Su, Q.; Jiang, Z. The Simulated Vibrational Spectra of HfO_2 Polymorphs. *J. Phys. D: Appl. Phys.* 2014, *47*, 115502.

(146) Perevalov, T.; Gritsenko, V.; Erenburg, S.; Badalyan, A.; Wong, H.; Kim, C. Atomic and Electronic Structure of Amorphous and Crystalline Hafnium Oxide: X-ray Photoelectron Spectroscopy and Density Functional Calculations. *J. Appl. Phys.* 2007, *101*, 053704.

(147) Van Humbeeck, J. Shape Memory Alloys: A Material and a Technology. *Adv. Eng. Mater.* 2001, 3, 837−850.

(148) Wang, L.; Xiong, Y.; Xiao, W.; Cheng, L.; Du, J.; Tu, H.; Van de Walle, A. Computational Investigation of the Phase Stability and the Electronic Properties for Gd-doped HfO_2. *Appl. Phys. Lett.* 2014, *104*, 201903.

(149) Zhao, X.; Vanderbilt, D. Phonons and Lattice Dielectric Properties of Zirconia. *Phys. Rev. B: Condens. Matter Mater. Phys.* 2002, *65*, 075105.

(150) Starschich, S.; Boettger, U. An Extensive Study of the Influence of Dopants on the Ferroelectric Properties of HfO_2. *J. Mater. Chem. C* 2017, *5*, 333−338.

(151) Guan, S.-H.; Zhang, X.-J.; Liu, Z.-P. Energy Landscape of Zirconia Phase Transitions. *J. Am. Chem. Soc.* 2015, *137*, 8010−8013.

(152) Depner, S. W.; Kort, K. R.; Banerjee, S. Precursor Control of Crystal Structure and Stoichiometry in Twin Metal Oxide Nanocrystals. *CrystEngComm* 2009, *11*, 841−846.

(153) Vioux, A. Nonhydrolytic Sol−Gel Routes to Oxides. *Chem. Mater.* 1997, *9*, 2292−2299.

(154) Kort, K. R.; Banerjee, S. Ligand-Mediated Control of Dislocation Dynamics and Resulting Particle Morphology of GdOCl Nanocrystals. *Small* 2015, *11*, 329−334.

(155) Kort, K. R.; Banerjee, S. Shape-Controlled Synthesis of Well-Defined Matlockite LnOCl (Ln: La, Ce, Gd, Dy) Nanocrystals by a Novel Non-Hydrolytic Approach. *Inorg. Chem.* 2011, *50*, 5539−5544.

(156) De Keukeleere, K.; Coucke, S.; De Canck, E.; Van Der Voort, P.; Delpech, F.; Coppel, Y.; Hens, Z.; Van Driessche, I.; Owen, J. S.; De

Roo, J. Stabilization of Colloidal Ti, Zr, and Hf Oxide Nanocrystals by Protonated Tri-*n*-octylphosphine Oxide (TOPO) and Its Decomposition Products. *Chem. Mater.* 2017, *29*, 10233−10242.
(157) Pitcher, M. W.; Ushakov, S. V.; Navrotsky, A.; Woodfield, B. F.; Li, G.; Boerio-Goates, J.; Tissue, B. M. Energy Crossovers in Nanocrystalline Zirconia. *J. Am. Ceram. Soc.* 2005, *88*, 160−167.
(158) Chevalier, J.; Gremillard, L.; Virkar, A. V.; Clarke, D. R. The Tetragonal-Monoclinic Transformation in Zirconia: Lessons Learned and Future Trends. *J. Am. Ceram. Soc.* 2009, *92*, 1901−1920.
(159) Lange, F. Transformation Toughening. *J. Mater. Sci.* 1982, *17*, 225−234.

DOI: 10.1021/acs.jpcc.8b04622
J. Phys. Chem. C XXXX, XXX, XXX−XXX